Boundary element formulation of axisymmetric problems in vertically non-homogeneous solids subject to normal traction

Sha Xiao, Zhongqi Quentin Yue*

Department of Civil Engineering, The University of Hong Kong, Hong Kong, PR China

Abstract

This paper presents an efficient and accurate boundary element method (BEM) for the elastic analysis of axisymmetric problems in vertically non-homogeneous solids without or with cavity. This BEM uses the fundamental solution of the elastic field in a multilayered elastic solid induced by the body force uniformly concentrated at a circular ring. This solution is also called Yue's solution. The effective integration methods are used for dealing with the integrals in the discretized boundary integral equations. The discretization of the boundary surface uses one-dimensional boundary elements. It also adopts the infinite boundary element to take into account the influence of a far-field region on the boundary surface. Numerical verifications of displacements and stresses for three benchmark problems are conducted, which gives the excellent agreement with previously published results. Case studies are presented to numerically illustrate the influences of both vertically non-homogeneous elastic material properties and spherical cavity on the elastic fields induced by uniform tractions on the boundary surface. These numerical results show that this new BEM is a fast and simple numerical algorithm for accurately computing the axisymmetric elastic fields in vertically non-homogeneous solids with or without cavity induced by normal tractions.

Keywords: BEM, axisymmetric problems, layered solids, vertically non-homogeneous solids, infinite elements, cavity

* Corresponding author: Z. Q. Yue, Email: yueqzq@hku.hk, Tel: +852-28591967

1. Introduction

1.1 Boundary element methods for homogeneous axisymmetric problems

This paper aims to present a new BEM for axisymmetric problems in vertically non-homogeneous elastic solids without or with a cavity (Fig. 1). Axisymmetric problems are often encountered in engineering and science since some structures and their loadings can be treated as axisymmetric. In particular, their dimensionality is reduced from three dimensions to two dimensions and includes only the radial and axial directions. The discretization of the boundary conditions for axisymmetric problems only needs one-dimensional (1-D) boundary elements, which makes their computations much simplified and straight forward.

Hence, the boundary element method (BEM) for axisymmetric problems appeared in the 1970s. Kermanidis [1] and Mayr [2] developed the earliest BEM for axisymmetric elasticity problems with the one-dimensional (1-D) constant or linear variation elements. They used the fundamental solution of a homogeneous isotropic elastic solid of infinite space subjected to circular ring loads. Then, Cruse et al. [3] extended the BEM for the analysis of the axisymmetric problem with thermal and rotational loading. Bakr and Fenner [4] presented the methods for treating the strongly singular integrals in the boundary integral equations for axisymmetric problems. Becker [5] described the boundary element techniques for axisymmetric problems in detail. Lacerda and Wrobel [6] and Mukherjee [7] presented axisymmetric hypersingular boundary integral formulations for elasticity problems and regularized the strongly singular and hypersingular equations. Ishida and Osaka [8] developed the formulation of the axisymmetric boundary integral equation for the transversely isotropic elastic solid. Amoura et al. [9] presented the dual boundary element method for the analysis of the cracks in axisymmetric structures. Lacerda and Wrobel [10] further developed the dual boundary element formulation for the evaluation of stress intensity factors and propagation of axisymmetric cracks.

Furthermore, the BEM is very effective in analyzing the problems in solids with fullspace or halfspace extent. For problems in halfspace solids, the boundary element formulation using the fundamental solution in the fullspace requires the discretization of the infinite free surface. In this case, infinite boundary elements can be introduced to consider the influence of the far field [11, 12]. Bu [13] developed the infinite boundary technique to analyze axisymmetric

halfspace problems. In these BEMs, the integration of the singular kernels over an infinite boundary element needs to be treated. An alternative way to deal with this problem is to implement the fundamental solution of a halfspace that satisfies in advance the traction free boundary condition on the free surface, which circumvents its numerical discretization on the traction free boundary surface. For example, Oliveira et al. [14] used the axisymmetric fundamental solution for an elastic halfspace to develop the BEM for the analysis of the elastic fields of homogeneous halfspaces with or without a shaped cavity.

1.2 Non-homogeneous solids and BEM issues

1.2.1 Non-homogeneous solids

The non-homogeneity of materials is a common phenomenon that can be observed in many natural and engineered materials. A homogeneous material is only an idealized case of heterogeneous materials in general. One special type of non-homogeneous materials is characterized by the variations of its physical and mechanical properties with the depth direction (i.e., the vertical z-axis). For example, the geotechnical investigations showed that the shear modulus of soils can vary linearly with depth [15, 16]. Using analytical methods, many investigations [17-26] have been done for the elastic responses of the vertically non-homogeneous halfspaces subjected to tractions or other types of loading conditions.

Another special type of non-homogeneous materials is characterized by layered structures. Sedimentary rock is a typical layered solid consisting of different rock layers [27]. Studies of specific interest to elastomechanics of layered halfspaces date back to the early studies by Chen [28], Yue and Wang [29], Pan [30], Alkasawneh et al. [31] and Pan et al. [32]. Recently, Xiao et al. [33] developed an analytical method of a layered halfspace subjected to interior loadings and assessed the additional elastic fields in the heterogeneous rocks beneath a reservoir due to its water weight loading.

On the other hand, cavities can exist in geometerials and may cause the shear or tensile failures under the action of loadings. For example, Yue [34] put forward a highly dense methane gas mass hypothesis in the crustal faults or cavities for the cause of tectonic earthquakes. Hence, the effect of cavity in non-homogeneous solids has to be considered for further analysis and

development.

1.2.2 BEMs for non-homogeneous solids

Further developments of BEM for axisymmetric problems in non-homogeneous solids, however, are limited because of the lack of the relevant fundamental solutions [35]. This situation can be observed in Pan [36] who recently provided a comprehensive literature review on the fundamental solutions or Green's functions in geophysics.

Particularly, Xiao et al. [37-39] developed new BEMs for the analysis of the 3D elastic fields of layered halfspaces and the stress intensity factor of the cracks in layered and graded solids. They incorporated the point-load fundamental solutions of layered solids into the BEM formulations. The point load fundamental solution is the elastic field in multi-layered solids subjected to the body force vector concentrated at a point. It was given by Yue [40-42] and also called as Yue's solution [43-45].

On the other hand, authors cannot find any papers using BEM for the analysis of axisymmetric elastic problems in vertically non-homogeneous solids published in the open literature in English and Chinese. Hence, this paper is to address this issue and to enrich the BEM.

1.3 Aim and approach of this study

The new BEM presented in the ensuing is for the analysis of axisymmetric problems in vertically non-homogeneous elastic solids without or with a cavity (Fig. 1). It adopts the fundamental solution of multilayered solids subjected to uniform ring body force vector concentrate along a circular ring. The fundamental solution is also derived by Yue [40-42]. This fundamental solution is used to eliminate the discretization task at the internal interfaces of non-homogeneous materials [46, 47].

Special attentions are also given to a fast numerical algorithm for computing the elastic fields induced by normal traction on vertically non-homogeneous halfspaces without or with a cavity. The algorithm is a single-region BEM. The infinite boundary element technique is used to take into account the influence of a far-field region on the boundary surface because of its

straightforward implementation. Various singular integrals involved in the discretized boundary integral equations are considered in detail.

The new BEM is applied to specifically solving the elastic responses of layered and vertically non-homogeneous halfspaces without or with a cavity under normal circular loads on the horizontal boundary surface. Numerical results show the influence of vertically non-homogeneous properties including elastic modulus and Poisson's ratio on the elastic displacement and stress fields induced by the normal tractions.

2. Boundary element formulation of axisymmetric elastostatic problems

2.1 Boundary integral equation for homogeneous materials

Axisymmetric geometries are formed by rotating the two-dimensional plane with the boundary *S*, shown in Fig. 2, through 360° about the *z*-axis (called the axis of rotational symmetry). Under an axisymmetric load, all displacements and stresses are independent of the hoop angle in the polar cylindrical coordinate system. For the axisymmetric homogeneous solid without body forces the boundary integral equation (BIE) is of the form [5]

$$c_{ij}(P)u_j(P)+2\pi\int_S t_{ij}^*(P,Q)u_j(Q)r_Q dS(Q)=2\pi\int_S u_{ij}^*(P,Q)t_j(Q)r_Q dS(Q) \quad (i,j=r,z) \qquad (1)$$

where P and Q are, respectively, the source and field points; t_j and u_j are, respectively, tractions and displacements; t_{ij}^* and u_{ij}^* are, respectively, the kernel functions of the tractions and displacements of the fundamental solution of a homogeneous fullspace subjected to circular ring loads; r_Q is the horizontal distance of the field point Q to the z-axis. The free term $c_{ij}(P)$ in Eq. (1) depends only upon the asymmetric behavior of the singular terms of the fundamental solution and the local geometry of the boundary at the source point P.

The boundary integral equation (1) is effective for the axisymmetric elastic problems in a homogeneous solid and can be extended to examine the axisymmetric elastic problems in vertically non-homogeneous materials. The extension needs the corresponding fundamental solution in vertically non-homogeneous solids.

2.2 Fundamental solutions of a multilayered solid subjected to circular ring loads

Yue [40-42] presented the fundamental solution of a multilayered elastic solid subjected to the body force vector uniformly concentrated along a horizontal circular ring. The total number of the dissimilar layers is an arbitrary integer *n*. The dissimilar homogeneous layers adhere an elastic solid of upper halfspace and another elastic solid of lower halfspace. The interface between any two connected dissimilar layers is fully bonded. By referring to Fig. 3, the *j*-th layer occupies a finite layer region $H_{j-1} \le z \le H$ of thickness h_j, and has the shear modulus μ_j and the Poisson's ratio ν_j, where *j*=1,2,3,…,*n*. The 0-th layer occupies the upper halfspace region $-\infty < z \le 0$, and has the shear modulus μ_0 and the Poisson's ratio ν_0. The (*n*+1)-th layer occupies the lower halfspace region $H_n \le z < \infty$ and has the shear modulus μ_{n+1} and the Poisson's ratio ν_{n+1}. Without loss of generality, it is assumed that the ring loads $\left(f_r, f_z\right)$ are concentrated along $r=r_Q$ at $z = d$ in the *k*-th layer. Numerical verifications illustrate that when applying this fundamental solution to the new BEM for finite domain or semi-infinite domain, the shear modules μ_0 and the Poisson's ratio ν_0 of the 0-th layer can be treated to be the same as those elastic parameters of the first layer (*j*=1) [48]. Furthermore, by assuming $\mu_0 = 0$, the fundamental solution is that of a (*n*+1) layered elastic solid of halfspace extent subject to the circular ring body force vector.

Some basic formulations of the fundamental solution are provided in Appendix A. The numerical results can be achieved with any pre-given accuracy. The convergence of the solution has been verified and the solution satisfies all the required conditions including the basic equations and the interfacial conditions as well as the loading conditions. It is verified that the singularities of the displacements and stresses of the fundamental solution are, respectively, of the forms ln(1/*r*) and 1/*r* for the ring type of concentrated forces (*r* is a distance between the source and field points), are exactly the same as those of the fundamental solutions in either a homogeneous solid or a bi-material solid of fullspace region.

2.3 Boundary integral equation for non-homogeneous materials

Using the fundamental solution of a multilayered elastic solid [40-42], the boundary integral equation (1) for axisymmetric problems can be re-expressed as follows:

$$c_{ij}(P)u_j(P)+2\pi\int_S t_{ij}^Y(P,Q)u_j(Q)r_Q dS(Q)=2\pi\int_S u_{ij}^Y(P,Q)t_j(Q)r_Q dS(Q)$$

$$(i,j=r,z) \qquad (2)$$

where t_{ij}^Y and u_{ij}^Y are, respectively, the kernel functions of the tractions and displacements of the fundamental solution of a layered fullspace subjected to circular ring loads; S is the boundary of the problem domain.

As shown in Fig. 4, an axisymmetric and layered halfspace formed by rotating the two-dimensional plane through 360° about the z-axis. Here, the boundary surface S of the two-dimensional plane is divided into two parts S_F and S_I. For the axisymmetric problems in layered halfspace without a cavity, the boundary S_F only represents the horizontal boundary surface of a halfspace. However, for the axisymmetric problems in layered halfspace with a cavity, the boundary S_F includes the horizontal boundary surface of a halfspace and the boundary of cavity. They represent a core region around the traction area and a far-field region beyond the traction area, respectively. In using the fundamental solution of a layered fullspace, $c_{ij}(P)=0.5\delta_{ij}$ for the point P located on a smooth boundary at a boundary surface.

2.4 Displacements and stresses in the domain

After obtaining the displacements and tractions on the boundary, the displacements at any internal point p can be determined by using the displacement integral equations as follows:

$$u_i(p)+2\pi\int_{S_F+S_I} t_{ij}^Y(p,Q)u_j(Q)r_Q dS(Q)=2\pi\int_{S_F+S_I} u_{ij}^Y(p,Q)t_j(Q)r_Q dS(Q)$$

$$(i,j=r,z) \qquad (3)$$

In the cylindrical coordinates (r,θ,z), the stresses of an axisymmetric solution domain can be expressed as [49]

$$\sigma_{rr}=2\mu\left[\frac{\partial u_r}{\partial r}+\frac{\nu}{1-2\nu}\left(\frac{\partial u_r}{\partial r}+\frac{u_r}{r}+\frac{\partial u_z}{\partial z}\right)\right] \qquad (4a)$$

$$\sigma_{zz} = 2\mu\left[\frac{\partial u_z}{\partial z} + \frac{\nu}{1-2\nu}\left(\frac{\partial u_r}{\partial r} + \frac{u_r}{r} + \frac{\partial u_z}{\partial z}\right)\right] \tag{4b}$$

$$\sigma_{rz} = \mu\left(\frac{\partial u_r}{\partial z} + \frac{\partial u_z}{\partial r}\right) \tag{4c}$$

$$\sigma_{\theta\theta} = 2\mu\left[\frac{u_r}{r} + \frac{\nu}{1-2\nu}\left(\frac{\partial u_r}{\partial r} + \frac{u_r}{r} + \frac{\partial u_z}{\partial z}\right)\right] \tag{4d}$$

Using Eq. (3), the differentials of the displacements with the coordinates (r, z) in Eq. (4) can be expressed as

$$u_{i,k}(p) + 2\pi\int_{S_F+S_I} t^Y_{ij,k}(p,Q)u_j(Q)r_Q dS(Q) = 2\pi\int_{S_F+S_I} u^Y_{ij,k}(p,Q)t_j(Q)r_Q dS(Q)$$

$$(i, j, k = r, z) \tag{5}$$

where $t^Y_{ij,k}$ and $u^Y_{ij,k}$ are the new kernel functions obtained from the displacements and stresses of the fundamental solution in a layered solid of fullspace and their values can be obtained using the difference formula shown in Appendix B.

3. Boundary element techniques for new BEM

3.1 The 1D finite boundary element

As shown in Fig. 4, the boundary surface can be divided into two regions S_F and S_I. Following the procedure of Xiao et al. [37], two types of boundary elements, ie, finite isoparametric and infinite boundary elements in one dimension (1D), are used to discretize the boundaries S_F and S_I, respectively. Accordingly, the two boundary element techniques are developed.

The conventional three-node finite isoparametric elements, shown in Fig. 5a, are employed to discretize the finite core region S_F. The shape functions of this type of elements are [5]

$$N_1(\xi) = -\frac{1}{2}\xi(1-\xi),\quad N_2(\xi) = (1+\xi)(1-\xi),\quad N_3(\xi) = \frac{1}{2}\xi(1+\xi) \tag{6}$$

The geometry of an isoparametric element can be defined by the coordinates of its three nodes as follows:

$$r(\xi)=\sum_{\alpha=1}^{3}N_\alpha(\xi)r^\alpha,\ \ z(\xi)=\sum_{\alpha=1}^{3}N_\alpha(\xi)z^\alpha \tag{7}$$

Similarly, because the elements are isoparametric, the same shape functions are used for the solution variables as follows:

$$u_i(\xi)=\sum_{\alpha=1}^{3}N_\alpha(\xi)u_i^\alpha,\ \ t_i(\xi)=\sum_{\alpha=1}^{3}N_\alpha(\xi)t_i^\alpha \quad (i=r,z) \tag{8}$$

3.2 The 1D infinite boundary element

A one-dimensional infinite element, shown in Fig. 5b, is employed to discretize the far-field region S_I of the boundary surface of the layered elastic halfspace. The shape functions of this type of elements shown by Moser et al. [47] are presented as follows:

$${}^{\infty}N_1(\xi)=-\frac{2\xi}{1-\xi},\ \ {}^{\infty}N_2(\xi)=\frac{1+\xi}{1-\xi} \tag{9}$$

The geometry of an infinite element can be defined by the coordinates of its two nodes as follows:

$$r(\xi)=\sum_{\alpha=1}^{2}{}^{\infty}N_\alpha(\xi)r^\alpha,\ \ z(\xi)=\sum_{\alpha=1}^{2}{}^{\infty}N_\alpha(\xi)z^\alpha \tag{10}$$

The interpolation functions of displacements and tractions within the infinite element are also presented as follows:

$${}^{\infty}N_1^u(\xi)=\frac{1}{2}(1-\xi),\ \ {}^{\infty}N_1^t(\xi)=\frac{1}{4}(1-\xi)^2 \tag{11}$$

where ${}^{\infty}N_1^u(\xi)$ and ${}^{\infty}N_1^t(\xi)$ are, respectively, the interpolation functions of displacements and tractions.

The variations of u_i and t_i within the infinite element can be described as follows:

$$u_i(\xi)={}^{\infty}N_1^u(\xi)u_i^1,\ \ t_i(\xi)={}^{\infty}N_1^t(\xi)t_i^1 \tag{12}$$

3.3 Discretized governing boundary integral equations

The above two 1D boundary elements are used for discretization of the boundary surface

S_F and S_I. The governing boundary integral equation (2) can be re-written as the following discretized expressions

$$\begin{aligned} c_{ij}(P)u_j(P)+2\pi\sum_{e=1}^{FBE}\int_{S_F^e}t_{ij}^Y(P,Q)u_j(Q)r_Q dS(Q)+2\pi\int_{S_I}t_{ij}^Y(P,Q)u_j(Q)r_Q dS(Q) \\ =2\pi\sum_{e=1}^{FBE}\int_{S_F^e}u_{ij}^Y(P,Q)t_j(Q)r_Q dS(Q)+2\pi\int_{S_I}u_{ij}^Y(P,Q)t_j(Q)r_Q dS(Q) \end{aligned} \tag{13}$$

where *FBE* is the numbers of finite isoparametric boundary elements and only one infinite boundary element is used to discretize the boundary surface S_I.

Using Eqs. (7), (8), (10) and (11), Eq. (13) can be further re-written as follows:

$$\begin{aligned} c_{ij}(P)u_j(P)+2\pi\sum_{e=1}^{FBE}\sum_{\alpha=1}^{3}u_j(Q^\alpha)\int_{S_F^e}t_{ij}^Y(P,Q)N_\alpha r_Q dS(Q)+2\pi u_j(Q^1)\int_{S_I}t_{ij}^Y(P,Q)^\infty N_1^u r_Q dS(Q) \\ =2\pi\sum_{e=1}^{FBE}\sum_{\alpha=1}^{3}t_j(Q^\alpha)\int_{S_F^e}u_{ij}^Y(P,Q)N_\alpha r_Q dS(Q)+2\pi t_j(Q^1)\int_{S_I}u_{ij}^Y(P,Q)^\infty N_1^t r_Q dS(Q) \end{aligned} \tag{14}$$

where the superscripts α and 1 of the field point *Q* are, respectively, the nodes α and 1 of finite isoparametric and infinite elements.

3.4 Evaluation of boundary stresses

The boundary stresses can be calculated directly using Eqs. (4) and (5). Because the kernel functions $t_{ij,k}^Y$ and $u_{ij,k}^Y$ in Eq. (5) are much complex, it requires a substantially higher computation time. The most popular technique for overcoming this difficulty is the traction recovery method. Xiao et al. [38] further developed this method to evaluate the boundary stresses of an inclined transversely isotropic bi-material. This method uses the tractions and displacements obtained by solving the discretized BIE (14), stress boundary conditions and the stress-strain relations. Herein, we extend this method for evaluating the stresses on the boundary surface of axisymmetric problems in layered halfspace.

4. Numerical integration

4.1 General

To set up a system of boundary integral equations, the integrals in Eq. (14) must be evaluated for each element and each local node of the element. For a finite isoparametric element, the following integrals $H_{ij}^{e\alpha}$ and $G_{ij}^{e\alpha}$ need to be considered

$$H_{ij}^{e\alpha} = \int_{S_F^e} u_{ij}^Y (P,Q) N_\alpha r_Q dS(Q) = \int_{-1}^{1} u_{ij}^Y (P,Q) N_\alpha r_Q J_1 d\xi \tag{15a}$$

$$G_{ij}^{e\alpha} = \int_{S_F^e} t_{ij}^Y (P,Q) N_\alpha r_Q dS(Q) = \int_{-1}^{1} t_{ij}^Y (P,Q) N_\alpha r_Q J_1 d\xi \tag{15b}$$

where the indexes *e* and α identify the element and node respectively, N^α is the shape function for a given node α in the element and J_1 is the Jacobian of transformation from the global coordinate system *Orz* to the local coordinate system $O\xi$.

For only an infinite element, the following integrals ${}^\infty H_{ij}$ and ${}^\infty G_{ij}$ at the local node 1 needs to be evaluated

$${}^\infty H_{ij} = \int_{S_I} u_{ij}^Y (P,Q) {}^\infty N_1^t r_Q dS(Q) = \int_{-1}^{1} u_{ij}^Y (P,Q) {}^\infty N_1^t r_Q J_1 d\xi \tag{16a}$$

$${}^\infty G_{ij} = \int_{S_I} t_{ij}^Y (P,Q) {}^\infty N_1^u r_Q dS(Q) = \int_{-1}^{1} t_{ij}^Y (P,Q) {}^\infty N_1^u r_Q J_1 d\xi \tag{16b}$$

Owing to singularity of the fundamental solution, an adequate numerical scheme must be adopted to these integrals. When *P* and *Q* are in different elements or *P* and *Q* are in the same element but $P \neq Q$, all integrals are regular and are evaluated by a classical Gaussian numerical quadrature. However, if *P* and *Q* are in the same element and *P=Q*, the integrals in Eqs. (15) and (16) are weakly or strongly singular. In the following, the techniques to treat these singular integrals are introduced.

4.2 Weakly singular integrals

In order to calculate the weakly singular integrals for the displacement kernel in Eqs. (15a) and (16a), the coordinate transformation is first performed from $\xi \in [-1,1]$ to $\eta \in [0,1]$. A simple linear transformation can be used to transform the integral variable from ξ to η as follows:

(1) If *P* is the first node of the element, ξ=-1+2η .

(2) If *P* is the second node of the element, the element is divided into two sub-elements: ξ=-η for -1 < ξ < 0 and ξ=η for 0 < ξ < -1.

(3) If *P* is the third node of the element, ξ =1-2η .

Now it is clear from Eqs. (15a) and (16a) that as *P* coincides with *Q*, the singularity of the integrand is of the form $\ln(1/\eta)$ as $\eta \to \infty$. In order to use the logarithmic Gaussian quadrature scheme, the following transformation of the integration in Eqs. (15a) and (16a) needs to be performed

$$\int_0^1 f(\eta)\,d\eta = \int_0^1 \frac{f(\eta)\ln(1/\eta)}{\ln(1/\eta)}\,d\eta = \int_0^1 h(\eta)\ln(1/\eta)\,d\eta = \sum_{gl=1}^{G_l} h(\eta_{gl})\,w_{gl} \tag{17}$$

The right-hand side of the above equation is exactly as required by the logarithmic Gaussian quadrature [5]. The 6-point numerical quadrature is used in the integral with respect to η in Eq. (17).

For Eqs. (15a) and (16a), the integrands in Eq. (17) are, respectively, given by

$$h(\eta) = u_{ij}^{Y}\left[P,Q(\eta)\right] N_{\alpha}(\eta)\, r_Q(\eta)\, J_1(\eta)\, J_2 / \ln(1/\eta) \tag{18a}$$

$$h(\eta) = u_{ij}^{Y}\left[P,Q(\eta)\right]^{\infty} N_1^t(\eta)\, r_Q(\eta)\, J_1(\eta)\, J_2 / \ln(1/\eta) \tag{18b}$$

where J_2 is the Jacobian of transformation from the coordinate system $O\xi$ to the coordinate system $O\eta$.

4.3 Strongly singular integrals

In classical axisymmetric BEM formulations using the fundamental solution of homogeneous solids, the strongly singular integrals related to the *z* direction can be indirectly evaluated using the rigid body motion method and the ones related to the *r* direction can be indirectly evaluated using prescribed tractions in the *r* and *z* directions and calculating the corresponding displacements [5]. Since the infinite boundary element is used in this BEM, the strongly singular integrals related to the *z* direction cannot be evaluated indirectly using the

rigid body motion method. Thus, an effective numerical method needs to be provided for calculating the strongly singular integral. In the following, a Kutt's numerical quadrature, suggested by Xiao et al. [37-39], is adopted to calculate the strongly singular integrals for the finite and infinite elements.

In order to calculate the strongly singular integrals for the traction kernel in Eqs. (15b) and (16b), the coordinate transformation presented in Section 4.2 is performed from $\xi \in [-1,1]$ to $\eta \in [0,1]$. Thus, these strongly singular integrals can be re-written as follows:

$$\int_0^1 F(\eta)d\eta = \int_0^1 \frac{F(\eta)\eta}{\eta} d\eta = \int_0^1 \frac{L(\eta)}{\eta} d\eta = \sum_{k=1}^{K} L\left(\frac{k-1}{K}\right) w_k \tag{19}$$

where w_k is the weight given by Kutt [50]. The Kutt's 10-point equispace quadrature is used in the finite-part integral with respect to η in Eq. (19).

For Eqs. (15b) and (16b), the integrands in Eq. (19) are given by

$$L(\eta) = t_{ij}^{Y}\left[P, Q(\eta)\right] N_{\alpha}(\eta) r_{Q}(\eta) J_1(\eta) J_2 \eta \tag{20a}$$

$$L(\eta) = t_{ij}^{Y}\left[P, Q(\eta)\right]^{\infty} N_1^{u}(\eta) r_{Q}(\eta) J_1(\eta) J_2 \eta \tag{20b}$$

4.4 Nearly singular integrals

In Eqs. (1), (2) and (3), when *P* lies close to but not in the element of *Q*, the kernels of displacements and tractions vary strongly as the distance from *P* to *Q* becomes small. It has been found that the accuracy of calculating this type of integrals is closely related to the ratio of the element length to the distance from a source point to the element. In this case, an element may be further divided into sub-regions to solve this type of integrals. Furthermore, the improved adaptive integration presented by Xiao et al. [38] is proposed to accurately and efficiently treat this type of integrals.

5. Numerical results and verifications

Based on the above analytical and numerical equations, a new BEM program in Fortran is made to calculate the axisymmetric elastostatic fields of displacements and stresses in vertically

non-homogeneous halfspaces due to tractions. This BEM program can calculate all the field variables at any point in the elastic halfspaces induced by axisymmetric tractions. In this section, several axisymmetric problems in layered and/or vertically non-homogeneous halfspaces are examined and presented to show (1) the high efficiency and accuracy can be achieved by the new BEM formulation and (2) the material heterogeneity can have profound effects on the elastic fields.

5.1 The first verification case

The first verification case is the classical axisymmetric problem of a homogeneous elastic halfspace subjected to a uniform normal traction p_0 over a circular area of radius a on its boundary surface. The analytical expression for the vertical displacement at the distance r from the center of the circular area on the boundary surface is given as follows [13]:

$$\frac{\mu u_z(r,0)}{p_0 a} = \frac{2(1-\nu)}{\pi}\int_0^{\frac{\pi}{2}} \sqrt{1-\frac{r^2}{a^2}\sin^2\theta}\, d\theta \tag{21}$$

where μ is the shear modulus and ν is the Poisson's ratio of the homogeneous elastic halfspace.

As shown in Fig. 6, the new BEM uses eight finite isoparametric elements and one infinite boundary element to describe the loaded boundary surface of the elastic halfspace. It also uses only the eight finite isopatametric elements to calculate the vertical displacement. Three sets of numerical results for the vertical displacements are plotted in Fig. 7.

The analytical results obtained from Eq. (21) and the BEM scheme with eight finite isoparametric and one infinite boundary element are almost identical. The maximum difference between these two sets of numerical results is 1.025%. The numerical results from the third BEM scheme with only the eight finite isoparametric elements (without the infinite boundary element) are less than the above two results, which shows the importance of the infinite boundary element technique.

5.2 The second verification case

The second verification case is the axisymmetric problem of a layered solid with two dissimilar layers and a halfspace subjected to an elliptical traction over a circular area of radius *a* [28]. The shear moduli for the three layered solids are given as $\mu_2 / \mu_1 = 0.5$ and $\mu_3 / \mu_1 = 1$. The Poisson ratios are $\nu_1 = \nu_2 = \nu_3 = 0.3$. The upper two layer thicknesses are $h_1 / a = 0.4$ and $h_2 / a = 0.4$. The quantities *a* and μ_1 (shear modulus) are taken to be unit length and unit pressure respectively. The elliptical traction is defined as

$$p(r) = p_0 \sqrt{1 - (r/a)^2} \tag{22}$$

Herein, the boundary mesh of eight finite isoparametric elements and one infinite boundary element in Fig. 6 is further used. Table 1 compares the two set values of the normal stress σ_{zz} / p_0 and the shear stress σ_{rr} / p_0 at upper and lower surfaces of the second layer interface (i.e., $z / a = 0.8 \pm 10^{-5}$). One set is given by Chen [28] and the other by the present BEM scheme. The maximum relative difference is 1.88%. Furthermore, the jumps of the σ_{zz} / p_0 across the material interface at *z/a* = 0.8 is 0.00004 (or 0.017% of the actual value). Such small relative errors and stress jumps indicate that the new BEM can be of high accuracy in calculating the stresses at internal points.

5.3 The third verification case

The third verification case is the axisymmetric problems of layered halfspace with two layers and a homogeneous halfspace subjected to a traction *p* over a circular region of radius *a*, shown in Fig. 8. The two layers and the halfspace are assigned the names: layer 1, layer 2 and layer 3. Pan and his co-workers [30-32] developed the software MultiSmart3D for pavement analysis. Following Pan et al. [32], the elastic moduli and Poisson's ratios and the layer thicknesses are given as follows: E_1=5GPa, E_2=30GPa, E_3=150GPa, $\nu_1 = 0.3$, $\nu_2 = 0.25$, $\nu_3 = 0.2$, $h_1 = 0.5\text{km}$, $h_2 = 5\text{km}$.

The results presented by Pan et al. [32] are used for the verification. The radius of the

loading circular region a=1km and the uniform normal load p_0=1kPa.The fundamental solution satisfies the fully bonded (or continuous) interfacial condition between two adjacent dissimilar material layers. Therefore, in using the proposed BEM, only the external boundary surface needs to be discretized and the material interfaces do not need to be discretized. Here, the twenty finite isoparametric elements and one infinite element are used to discretize the boundary surface, as shown in Fig. 9. Fig. 10 illustrates the radial and vertical displacements (u_r and u_z) on the boundary surface. The radial and vertical displacements in Fig. 10 have completely the same tendency as the one in Fig. 3 of Pan et al. [32]. The present BEM program gives the vertical displacement of 0.012177 cm at the center of the loaded circular area (r=0) and the radial displacement of -0.0017105 cm at the boundary of the loaded circular area (r=1km). The displacements at these two points are 0.01221 cm and -0.001681 cm, respectively [32]. The maximum relative difference between the present numerical results and the exact results is 1.75%.

Pan et al. [32] presented only the surface deformation of a layered elastic halfspace due to a uniform normal traction over a circular area. Herein, we use the proposed BEM method to further calculate the displacements and stresses within the layered halfspaces subjected to uniform tractions over circular areas in the following Sections 5.4.

5.4 The further results of the third verification case

5.4.1 A layered halfspace subject to uniform traction on the boundary surface

In order to obtain the highly accurate solutions of displacements and stresses at the points close to the horizontal boundary surface, the adaptive numerical integration method is adopted. Furthermore, more elements are used to discretize the boundary near the internal points. As shown in Fig. 11, the axisymmetric boundary surface of a halfspace is discretized by sixty finite elements and one infinite element. Five different discretizations presented in Fig.11 are applied when the radial coordinates of internal points are equal to $0,\ 0.5,\ 1,\ 1.5,\ 2$ km, respectively. For easy reference, the organizations of all numerical examples in Sections 5.4, 5.5 and 6 are summarized in Table 2.

The first new results are the elastic fields of a non-homogeneous halfspace with two dissimilar layers and a homogeneous halfspace subjected to a uniform normal traction p_0 over a circular area. All five different boundary discretizations shown in Fig. 11 are applied for internal points whose radial coordinates $r = 0,\ 0.5,\ 1,\ 1.5,\ 2$ km, respectively. In addition, Fig. 11c is also used for the internal points whose radial coordinates $r = 0.95,\ 1.05$ km.

Figs. 12a and 12b shows the depth variations of the horizontal and vertical displacements (u_r and u_z) along four and five radial locations of the two-layered halfspace, respectively. The two displacements (u_r and u_z) are non-smoothly continuous across the material interfaces at *z*=0.5 and 5.5 km. As would be expected, all the displacements decrease with *r* and *z* increasing and vary obviously in the first layer.

Figs. 13a, 13b, 13c, and 13d shows the depth variations of the four stress components (σ_{rr}, $\sigma_{\theta\theta}$, σ_{zz}, σ_{rz}) along five radial locations of the two-layered halfspace, respectively. Notice that the shear stress components ($\sigma_{r\theta}$ and $\sigma_{\theta z}$) in axisymmetric problems are equal to zero. The plane stresses (σ_{rr} and $\sigma_{\theta\theta}$) are discontinuous across the material interfaces at *z* = 0.5 and 5.5 km whereas the vertical stresses (σ_{zz} and σ_{rz}) are non-smoothly continuous across the material interfaces *z* = 0.5 and 5.5 km. The stress jumps of σ_{rr} at *z* = 0.5 km are, respectively, 0.05347, 0.089823, 0.00961, 0.05636 and 0.00585 kPa for *r*=0, 0.5, 1, 1.5 and 2 km. The jumps of $\sigma_{\theta\theta}$ at *z* = 0.5 km are, respectively, 0.053505, 0.071621, 0.02368, 0.03813 and 0.02630 kPa for *r* = 0, 0.5, 1, 1.5 and 2 km. At *z* = 5.5 km, the stress jumps of σ_{rr} ($\sigma_{\theta\theta}$) for *r* = 0, 0.5, 1, 1.5 and 2 km are 0.017168, 0.016458, 0.014483, 0.011608 and 0.0083260 kPa (0.017168, 0.016761, 0.015603, 0.013868 and 0.011800 kPa), respectively. As *z* tends to zero, the stress of σ_{zz} approaches 1 kPa for *r* = 0 and 0.5 km and approaches 0.5 kPa for *r* = 1 km, which can indicate that the proposed adaptive integration is of high accuracy, and the numerical methods of calculating the stresses on the boundary surface and within the halfspace are effective and correct.

On the horizontal surface $z = 0$, the shear stress σ_{rz} is equal to zero. σ_{rz} approaches zero as z tends to zero. Fig. 13d presents the variations of σ_{rz} at r = 0.95 and 1.05 km along the z-direction. It can be found that σ_{rz} varies violently in the neighborhood of r = 1 km and z = 0.

5.4.2 A layered halfspace with a spherical cavity and subject to uniform traction on boundary surface

In this section, the layered elastic halfspace with a spherical cavity, shown in Fig. 14, is analyzed. The halfspace is subjected to a uniform vertical load p_0 on a circular area with a radius of a=1 km. The spherical cavity has a radius R=1 km and is located within the layer 2. Fig. 15 shows the discretization mesh on the boundary surface ($z = 0$ and $r \geq 0$) and the boundary of the spherical cavity ($r \geq 0$). The mesh of the horizontal boundary is the same as the one shown in Fig. 9. The local spherical coordinate system ($O'R\ \varphi$), shown in Fig. 15, needs to be established to describe the radial and hoop displacements on the boundary of the spherical cavity.

Fig. 16a and Fig. 16b respectively give the variations of the horizontal and vertical displacements on the boundary surface $z = 0$ for the different distances of the spherical cavity to the boundary surface (d_s/a = 2, 2.5, 3, 3.5 and 4). As the distance d_s of the center of the spherical cavity to the horizontal boundary decreases, both the horizontal displacement u_r and the vertical displacement u_z increase. For d_s/a = 4, the two displacements with the cavity are close to those without the cavity. At r/a = 1, u_r has its peak values of -0.021763, -0.019617, -0.018232, -0.017653, -0.017386 and -0.017105 mm for d_s/a = 2, 2.5, 3, 3.5, 4 and ∞, respectively. At r/a = 0, u_z has its peak values of 0.14190, 0.12917, 0.12522, 0.12361, 0.12284 and 0.12173 mm for d_s/a = 2, 2.5, 3, 3.5, 4 and ∞, respectively. These values quantitatively show the effect of the cavity to the ground displacements. Note, the case $d_s/a = \infty$ equals to the case without cavity.

Fig. 17a and Fig. 17b respectively illustrate the radial displacements u_R and the hoop displacement u_φ on the boundary of the spherical cavity. At a given d_s value, the u_R has its maximum inward value at the hoop angle $\varphi = 0°$. Then as φ increases the inward value of u_R decreases to zero at φ_0=74.70°, 75.45°, 76.03°, 76.56°, 77.21° for d_s/a = 2, 2.5, 3, 3.5 and 4,

respectively. After these angles, the u_R changes to displace outward and its outward value increases as φ increases to 180°. Secondly, the inward and outward values of u_R at any value of φ ($0° \le \varphi < \varphi_0$ and $\varphi_0 < \varphi \le 180°$) decrease, but its zero value keeps at $\varphi = \varphi_0$, as the distance d_s increases from $2a$ to $4a$. At φ = 0°, u_R has its inward peak values of -0.071497, -0.043210, -0.029790, -0.021749 and -0.016406 mm for d_s/a = 2, 2.5, 3, 3.5 and 4, respectively. At φ = 180°, u_R has its outward peak values of 0.0052921, 0.0040745, 0.0030650, 0.0023056 and 0.0019059 mm for d_s/a = 2, 2.5, 3, 3.5 and 4, respectively. These peak values show the importance of the distance of the cavity to the traction at the ground.

Thirdly, at a given d_s value, the hoop displacement u_φ is along the clock-wise direction and its value increases from zero to a peak value and then decreases to zero as φ increases from 0° to 180°. At the peak value, φ is about 39.38° for d_s/a = 2 and 2.5, 45° for 3, 3.5 and 4. Fourthly, as d_s increases, u_φ decreases for any value of φ ($0° < \varphi < 180°$). At φ = 39.38° or 45°, u_φ has its peak values of 0.034293, 0.022810, 0.016612, 0.012563 and 0.0096641 mm for d_s/a = 2, 2.5, 3, 3.5 and 4, respectively.

6. Numerical results and analyses of new applications

6.1 The vertically non-homogeneous solids and their n-layer approximation

The new examples given below are to analyze the elastic fields of four types of vertically non-homogeneous solids subjected to uniform (or elliptical) normal tractions over circular areas. As shown in Fig. 18, the elastic modulus $E(z)$ and the Poisson's ratio $\nu(z)$ of the non-homogeneous solid vary with depth z. According to Selvadurai and Katebi [25] and Katebi and Selvadurai [26], this paper assumes $E(z)$ and $\nu(z)$ as follows:

$$E(z) = E_0 e^{\lambda_1 z}, \quad z < H \quad \text{and} \quad E(z) = E_0 e^{\lambda_1 H}, \quad z \ge H \tag{23a}$$

$$\nu(z) = \nu_0 e^{\lambda_2 z}, \quad z < H \text{ and } \nu(z) = \nu_0 e^{\lambda_2 H}, \quad z \ge H \tag{23b}$$

where λ_1 and λ_2 are, respectively, the heterogeneous parameters of the elastic modulus and the Poisson's ratio. Eq. (23a) and Eq. (23b) show that the elastic modulus and the Poisson's ratio vary with depth when $z < H$ and keeps constant when $z \ge H$. It is noted that

$-1 < \nu(z) \le 0.5$ for the selection of λ_2. Furthermore, it is assumed that $H = a$ in the following calculations.

As shown in Fig. 19, for $0 \le z \le H$, the vertically non-homogeneous solid can be closely approximated with n fully bonded dissimilar layers. Each layer has the thickness of H/n. For the i-th layer, $E(z) = E(z_i)$ and $\nu(z) = \nu(z_i)$, $z = iH/n$ and $i = 1, 2, 3, \cdots, n$. A close approximation of the arbitrary depth variation of elastic modulus and Poisson's ratio can be obtained as the layer number n is large.

Fig. 20 presents the variations of the vertical displacement $u_z(r,0)E_0 / p_0 a$ with the radial distance r/a for dissimilar layer number n = 5, 10, 20, 30, 40 and 50, respectively. The traction boundary is discretized with the eight finite elements and one infinite element as given in Fig. 6. The n can affect the vertical displacement. For n = 5, 10, 20, 30, 40 and 50, the maximum values of $u_z(r,0)E_0 / p_0 a$ at r/a = 0 in Fig. 20a (or Fig. 20b) are 0.94509, 0.91776, 0.90785, 0.90704, 0.89877 and 0.89692 (or 1.9303, 1.9269, 1.9248, 1.9248, 1.9242 and 1.9275), respectively. Similar to the results presented by Xiao et al. [39], when n = 50, stable displacement values can be obtained. So, n = 50 is used to calculate the elastic field of the vertically non-homogeneous halfspace in the ensuing.

6.2 Vertically non-homogeneous halfspaces subjected to uniform traction

6.2.1 First case of different λ_1 values and $\lambda_2 = 0$

The first case is to investigate the variations of displacements and stresses for different λ_1 values of the non-homogeneous solid. The boundary discretization mesh given in Fig. 11a is used. λ_1 is given six different values of 0.0, 0.1, 0.25, 0.5, 1.0, and 1.5, respectively. The Poisson's ratio $\nu(z) = 0.3$.

Figs. 21a and 21b show the vertical displacements $u_z(0,z)E_0 / p_0 a$ and $u_z(r,0)E_0 / p_0 a$ as functions of z/a and r/a, respectively. Both $u_z(0,z)E_0 / p_0 a$ and $u_z(r,0)E_0 / p_0 a$

decrease as λ_1 increases.

Figs 22a and 22b illustrate the radial normal stress $\sigma_{rr}(0,z)/p_0$ and the vertical normal stress $\sigma_{zz}(0,z)/p_0$ as functions of z/a along the z-axis at $r = 0$, respectively. They show that the λ_1 can strongly affect $\sigma_{rr}(0,z)/p_0$ and slightly affect $\sigma_{zz}(0,z)/p_0$. At z=0.35a, $\sigma_{rr}(0,z)/p_0$ keep the same value of -0.40 in tension for the 6 different values of λ_1. When z<0.3a, the value of $\sigma_{rr}(0,z)/p_0$ in tension decreases as λ_1 increases. When z>0.3a, the value of $\sigma_{rr}(0,z)/p_0$ in tension increases as λ_1 increases. However, the value of $\sigma_{zz}(0,z)/p_0$ is always in compression and decreases as λ_1 increases.

In general, $u_z(0,z)E_0/p_0a$, $\sigma_{rr}(0,z)/p_0$, and $\sigma_{zz}(0,z)/p_0$ are smoothly continuous with z/a except at the material interface z/a =1, where they are non-smoothly continuous. The $\sigma_{rr}(0,z)/p_0$ becomes non-smoothly continuous at the interface because the material properties are the same across the interface.

6.2.2 Second case of different ν_0 values at λ_1=1.0 and λ_2 = 0

The second case is to investigate the variations of displacements and stresses for different Poisson's ratios of non-homogeneous halfspaces with elastic modulus varying with depth. The mesh in Fig. 11a is used again. The Poisson's ratio $\nu(z)=\nu_0=0$, 0.1, 0.2, 0.3, 0.4 and 0.5, respectively and the modulus $E(z)=E_0e^z$ for the case of $\lambda_1=1$.

Fig. 23 shows $u_z(0,z)E_0/p_0a$ as functions of z/a for six different values of Poisson's ratios. $u_z(0,z)E_0/p_0a$ decreases as Poisson's ratio increases at any given z/a and as z/a increases at any Poisson's ratio value.

Fig. 24a and Fig. 24b illustrate the radial normal stress $\sigma_{rr}(0,z)/p_0$ and the vertical normal stress $\sigma_{zz}(0,z)/p_0$ as functions of z/a along the z-axis at $r = 0$ for the six Poisson's ratio values, respectively. It is evident that the Poisson's ratio value can strongly affect

$\sigma_{rr}(0,z)/p_0$ and slightly affect $\sigma_{zz}(0,z)/p_0$. The value of $\sigma_{rr}(0,z)/p_0$ in tension increases as the Poisson's ratio value increases from 0 to 0.5 at any fixed depth *z*/*a*, and decreases as *z*/*a* increases at a fixed Poisson's ratio value. The value of $\sigma_{zz}(0,z)/p_0$ in compression increases as the Poisson's ratio value increases from 0 to 0.5 at any fixed depth *z*/*a*, and decreases as *z*/*a* increases at a fixed Poisson's ratio value.

6.2.3 Third case of different λ_2 *values and* $\lambda_1 = 0$

The third case is to investigate the variations of displacements and stresses for different λ_2 of non-homogeneous solid with Poisson's ratio varying with depth. The mesh in Fig. 11b is used. The heterogeneous parameter of the Poisson's ratio λ_2 is assumed to equal to 0, 0.5, 1 and 1.5. $\nu_0 = 0.1$ and $E(z) = E_0$ for $\lambda_1 = 0$.

Fig. 25a and Fig.25b show the horizontal radial displacement $u_r(0.5a,z)E_0/p_0a$ and the vertical displacement $u_z(0.5a,z)E_0/p_0a$ as the functions of *z*/*a* at the four values of λ_2, respectively. They show evidently that the λ_2 values can strongly affect $u_r(0.5a,z)E_0/p_0a$ and slightly affect $u_z(0.5a,z)E_0/p_0a$. In Fig. 25a, at a fixed λ_2 value, the value of $u_r(0.5a,z)E_0/p_0a$ has (1) its maximum negative value for *z*/*a* at 0, (2) then increases to zero as *z*/*a* increases from 0 to about 0.5, (3) then increases positively to its maximum positive value as *z*/*a* increases about 0.5 to 1 (the interface), and (4) then decreases positively to zero value as *z*/*a* increases 1 to infinite. At a fixed *z*/*a* value, the value of $u_r(0.5a,z)E_0/p_0a$ increases as λ_2 increases from 0 to 1.5. In Fig. 25b, $u_z(0.5a,z)E_0/p_0a$ decreases rapidly as *z*/*a* increases and increases very slightly as λ_2 increases from 0 to 1.5.

Fig. 26a, Fig. 26b and Fig. 26c illustrate the radial normal stress $\sigma_{rr}(0.5a,z)/p_0$, the vertical normal stress $\sigma_{zz}(0.5a,z)/p_0$, and the radial shear stress $\sigma_{rz}(0.5a,z)/p_0$ as

functions of z/a along the z-axis at r = 0.5a for the four λ_2 values, respectively. Similar to the above observations, the λ_2 values can affect strongly $\sigma_{rr}(0.5a,z)/p_0$, slightly $\sigma_{rz}(0.5a,z)/p_0$ and very slightly $\sigma_{zz}(0.5a,z)/p_0$. In Fig. 26a, $\sigma_{rr}(0.5a,z)/p_0$ changes significantly as z/a between 0.5 and 3. In Fig. 26c, $\sigma_{rz}(0.5a,z)/p_0$ varies noticeably as z/a between 0.5 and 1.3.

In general, $u_r(0.5a,z)E_0/p_0a$, $u_z(0.5a,z)E_0/p_0a$, $\sigma_{rr}(0.5a,z)/p_0$, $\sigma_{zz}(0.5a,z)/p_0$, and $\sigma_{rz}(0.5a,z)/p_0$ are smoothly continuous with z/a except at the material interface z/a=1, where they are non-smoothly continuous. The $\sigma_{rr}(0.5a,z)/p_0$ becomes non-smoothly continuous at the interface because the material properties are the same across the interface.

6.3 Effect of a spherical cavity in a vertically non-homogeneous halfspace

The new BEM is further applied to the analysis of a non-homogeneous elastic halfspace a spherical cavity, as shown in Fig. 27 in this sub-section. The halfspace is subjected to a uniform vertical load p_0 on a circular area with a radius of a. The elastic modulus varies with depth ($\lambda_1 = 1$) and the Poisson's ratio keeps constant with depth ($\nu_0 = 0.3$ and $\lambda_2 = 0$). The spherical cavity with a radius of a is completely within the lower homogeneous solid. The discretization mesh in Fig. 15 is further used here. Similar to those given in sub-sub-section 5.4.2, the results of this case are given and analyzed below.

Fig. 28a and Fig. 28b respectively give the variations of the horizontal radial displacement $u_r(r,0)E_0/p_0a$ and the vertical displacement $u_z(r,0)E_0/p_0a$ on the horizontal boundary z = 0 as functions of r/a, where d_s/a = 2, 2.5, 3, 3.5, 4 and ∞. As d_s/a decreases, both $u_r(r,0)E_0/p_0a$ and $u_z(r,0)E_0/p_0a$ increase. For d_s/a = 4, they are close to those without the cavity. At r/a = 1, $u_r(r,0)E_0/p_0a$ has its peak values of -0.18111, -0.14842, -0.13599, -0.13076, -0.12838 and -0.12560 for d_s/a = 2, 2.5, 3, 3.5, 4 and ∞, respectively. At r/a=0, $u_z(r,0)E_0/p_0a$ has its peak values of 1.08760, 0.96789, 0.93568, 0.91503, 0.90964 and

0.89950 for d_s/a = 2, 2.5, 3, 3.5, 4 and ∞, respectively. These values quantitatively show the effect of the cavity to the ground displacements. Note, the case $d_s/a = \infty$ equals to the case without cavity.

Fig. 29a and Fig. 29b illustrate the radial displacements $u_R(a,\varphi)E_0 / p_0 a$ and the hoop displacement $u_\varphi(a,\varphi)E_0 / p_0 a$ on the internal boundary of the spherical cavity. At a given d_s value, the $u_R(a,\varphi)E_0 / p_0 a$ has its maximum inward value at φ = 0°. Then as φ increases the inward value of $u_R(a,\varphi)E_0 / p_0 a$ decreases to zero at φ_0 =78.64°, 79.88°, 81.21°, 82.02° and 82.87° for d_s/a = 2, 2.5, 3, 3.5 and 4, respectively. After these angles, the $u_R(a,\varphi)E_0 / p_0 a$ changes to displace outward and its outward value increases as φ increases to 180°. Secondly, the inward and outward values of $u_R(a,\varphi)E_0 / p_0 a$ at any value of φ ($0° \le \varphi < \varphi_0$ and $\varphi_0 < \varphi \le 180°$) decrease, but its zero value keeps at $\varphi = \varphi_0$, as the distance d_s increases from 2a to 4a. At φ = 0°, $u_R(a,\varphi)E_0 / p_0 a$ has its inward peak values of -0.79605, -0.52227, -0.38444, -0.30130 and -0.24595 for d_s/a = 2, 2.5, 3, 3.5 and 4, respectively. At φ = 180°, $u_R(a,\varphi)E_0 / p_0 a$ has its outward peak values of 0.12757, 0.11596, 0.10594, 0.09731 and 0.08992 for d_s/a = 2, 2.5, 3, 3.5 and 4, respectively. These peak values show the importance of the distance of the cavity to the traction at the ground.

Thirdly, at a given d_s value, the hoop displacement $u_\varphi(a,\varphi)E_0 / p_0 a$ is along the clock-wise direction and its value increases from zero to a peak value and then decreases to zero as φ increases from 0° to 180°. At the peak value, φ is 39.38° for d_s/a = 2, 45° for d_s/a = 2.5, 50.62° for d_s/a=3, 56.25° for d_s/a = 3.5 and 4. Fourthly, as d_s increases, $u_\varphi(a,\varphi)E_0 / p_0 a$ decreases for any value of φ ($0° < \varphi < 180°$). At φ = 39.38°, 45°, 50.62°, 56.25° and 56.25°, $u_\varphi(a,\varphi)E_0 / p_0 a$ has its peak values of 0.39409, 0.28629, 0.22535, 0.18601 and 0.15876 for d_s/a = 2, 2.5, 3, 3.5 and 4, respectively.

7. Conclusions

In this paper, a new BEM has been developed for accurately and efficiently analyzing the axisymmetric elasticity problems in vertically non-homogeneous solids without or with a cavity subject to uniform tractions on boundary surfaces. The elastic properties of vertically non-homogeneous solids exhibit arbitrary variations in depth and keep constant in lateral directions. The new BEM is applicable to those special cases that both the structures and the loadings are symmetrical at the vertical axis *z*. For some axisymmetric geometries under non-axisymmetric loads, contact problems and fracture mechanics, special treatments are necessary. The key findings of the new BEM analysis are listed in Table 3. Further BEM analysis of axisymmetric problems of finite extent such as elliptical solid and hollow cylinder will be presented in future publications.

Acknowledgements

The work described in this paper was supported by the Research Grants Council of Hong Kong SAR Government (GRF Nos. 17204415 and 17207518). The authors are much grateful to the reviewers for their valuable comments and suggestions.

Appendix A. The basic formulations of the fundamental solution of a layered solid subjected to circular ring loads

The fundamental solutions $t_{ij}^{Y}(P,Q)$ and $u_{ij}^{Y}(P,Q)$ for a multilayered elastic solid, shown in Eq. (2), may be expressed as

$$t_{ij}^{Y}(P,Q)=\sigma_{jk}(P,Q)\big|_{f_i=1}\, n_k(Q) \qquad (i,j,k=r,z) \tag{A.1}$$

$$u_{ij}^{Y}(P,Q)=u_j(P,Q)\big|_{f_i=1} \qquad (i,j=r,z) \tag{A.2}$$

where f_i is a circular ring load acted at the source point $P(r,z)$ along the i direction, $\sigma_{jk}(P,Q)\big|_{f_i=1}$ and $u_j(P,Q)\big|_{f_i=1}$ are, respectively, the stresses and displacements at the field

source $Q(r,z)$ induced by the circular ring load f_i and $n_k(Q)$ is the outward normal component of the field point *Q*.

Yue [40-42] utilized classical integral transforms and a backward transfer matrix method to develop the closed-form fundamental solution of the stresses $\sigma_{jk}(P,Q)$ and displacements $u_j(P,Q)$ in Eqs. (A.1) and (A.2). For completeness, the essential formulations are presented in the ensuing. Note that the fundamental solution of a layered solid subjected to the concentrated load f_θ along the hoop direction is also presented in Yue [40-42].

The corresponding fundamental singular solutions of the layered solid due to the body force vector uniformly concentrated on the circular ring, ie, $\mathbf{f}_c = \begin{pmatrix} f_r & f_\theta & f_z \end{pmatrix}^{\mathrm{T}}$, can be expressed as follows:

$$\mathbf{u}(r,r_0,z) = \begin{pmatrix} u_r & u_\theta & u_z \end{pmatrix}^{\mathrm{T}} = \frac{1}{2\pi}\mathbf{G}_{u0}(r,r_0,z)\mathbf{f}_c \tag{A.3}$$

$$\mathbf{T}_z(r,r_0,z) = \begin{pmatrix} \sigma_{rz} & \sigma_{\theta z} & \sigma_{zz} \end{pmatrix}^{\mathrm{T}} = \frac{1}{2\pi}\mathbf{G}_{z0}(r,r_0,z)\mathbf{f}_c \tag{A.4}$$

$$\mathbf{\Gamma}_p(r,r_0,z) = \begin{pmatrix} \varepsilon_{rr} & \varepsilon_{r\theta} & \varepsilon_{\theta\theta} \end{pmatrix}^{\mathrm{T}} = \frac{1}{2\pi}\mathbf{G}_{p0}(r,r_0,z)\mathbf{f}_c \tag{A.5}$$

where r_0 is the radius of the ring loads, (r,z) is the coordinate of a field point, and the Green's functions in matrix form are defined as follows:

$$\mathbf{G}_{u0}(r,r_0,z) = \frac{1}{2\pi}\int_0^{+\infty} \mathbf{\Pi}_{c0}(\rho r)\mathbf{\Phi}(\rho,z)\mathbf{\Pi}_{c0}^{*}(\rho r_0)\,d\rho \tag{A.6}$$

$$\mathbf{G}_{z0}(r,r_0,z) = \frac{1}{2\pi}\int_0^{+\infty} \mathbf{\Pi}_{c0}(\rho r)\mathbf{\Psi}(\rho,z)\mathbf{\Pi}_{c0}^{*}(\rho r_0)\,d\rho \tag{A.7}$$

$$\mathbf{G}_{p0}(r,r_0,z) = \frac{1}{2\pi}\int_0^{+\infty} \mathbf{\Pi}_{cp0}(\rho r)\mathbf{\Phi}(\rho,z)\mathbf{\Pi}_{c0}^{*}(\rho r_0)\,d\rho \tag{A.8}$$

where

$$\mathbf{\Pi}_{c0}(\rho r) = \begin{bmatrix} -J_1(\rho r) & 0 & 0 \\ 0 & J_1(\rho r) & 0 \\ 0 & 0 & -J_0(\rho r) \end{bmatrix} = \mathbf{\Pi}_{c0}^{*}(\rho r) \tag{A.9}$$

$$\mathbf{\Pi}_{cp0}(\rho r) = -\frac{1}{2}\begin{bmatrix} J_0(\rho r) - J_2(\rho r) & 0 & 0 \\ 0 & J_2(\rho r) & 0 \\ J_0(\rho r) + J_2(\rho r) & 0 & 0 \end{bmatrix} = \mathbf{\Pi}^*_{c0}(\rho r) \tag{A.10}$$

The $J_0(\rho r)$, $J_1(\rho r)$ and $J_2(\rho r)$ are the Bessel functions of orders 0, 1 and 2, respectively. The basic solution matrices $\mathbf{\Phi}(\rho, z)$ and $\mathbf{\Psi}(\rho, z)$ are related only to the material properties of the *n*-layered solids and can be further expressed as

$$\mathbf{\Phi} = \begin{pmatrix} \Phi_{11}(\rho, z) & 0 & \Phi_{13}(\rho, z) \\ 0 & \Phi_{22}(\rho, z) & 0 \\ \Phi_{31}(\rho, z) & 0 & \Phi_{33}(\rho, z) \end{pmatrix} \tag{A.11}$$

$$\mathbf{\Psi} = \begin{pmatrix} \Psi_{11}(\rho, z) & 0 & \Psi_{13}(\rho, z) \\ 0 & \Psi_{22}(\rho, z) & 0 \\ \Psi_{31}(\rho, z) & 0 & \Psi_{33}(\rho, z) \end{pmatrix} \tag{A.12}$$

A rigorous mathematical verification has been conducted for the convergence and properties of the solutions expressed in the forms of inverse integral transforms. The ten fundamental functions in Eqs. (A.12) and (A.13) are continuous functions of the integral variables $\rho(0 \le \rho < \infty)$ and the depth $z(0 \le z < \infty)$ except that Ψ_{11}, Ψ_{22} and Ψ_{33} have a unit step decrease at $z=d$ and that they have no functions of exponential growth. The unit step decrease of Ψ_{11}, Ψ_{22} and Ψ_{33} at $z=d$ is due to the presence of the point loads at $z=d$. In addition, as the integral variable ρ approaches to infinity, the ten fundamental functions quickly vanish to zero by following $e^{-\rho|z-d|}$ for $|z-d| \ge \delta$, where δ is a positive small number. For $|z-d| < \delta$, a special treatment is needed to isolate the singular terms in the improper integrals of (A.6) to (A.8) [40-42].

A proceeding limit technique, based on an adaptively iterative Simpson's quadrature, is adopted in the evaluation of the inverse Hankel transform integrals in Eqs. (A.6) - (A.8). Using the procedure, the semi-infinite interval of the inverse Hankel transform integrals can be accommodated and the improper integrals can be efficiently evaluated with high and controlled accuracy.

It is noted that the solutions of the plane stresses ($\sigma_{rr}, \sigma_{r\theta}, \sigma_{\theta\theta}$) and the vertical strains

($\varepsilon_{rz}, \varepsilon_{\theta z}, \varepsilon_{zz}$) due to the ring loads f_r, f_θ and f_z can be easily obtained from the solutions of the vertical stresses ($\sigma_{rz}, \sigma_{\theta z}, \sigma_{zz}$) and the plane strains ($\varepsilon_{rr}, \varepsilon_{r\theta}, \varepsilon_{\theta\theta}$) by using the constitutive equations. More details of the expressions and mathematical properties of the fundamental solution can be found in Yue [40-42].

Appendix B. The kernel functions $u^Y_{ij,k}$ and $t^Y_{ij,k}$

The new kernels $u^Y_{ij,k}$ and $t^Y_{ij,k}$ in Eq. (2) can be approximated using difference formula as follows:

$$\frac{\partial u^Y_{ij}}{\partial r} \approx \frac{1}{2D}\left[u^Y_{ij}(r+D,z) - u^Y_{ij}(r-D,z)\right] \tag{B.1}$$

$$\frac{\partial u^Y_{ij}}{\partial z} \approx \frac{1}{2D}\left[u^Y_{ij}(r,z+D) - u^Y_{ij}(r,z-D)\right] \tag{B.2}$$

where r and z are the coordinates of the source point p in the global coordinate system and D is the distance between the two source points. The derivatives $t^Y_{ij,k}$ of the tractions can also be calculated using the above methods.

When the source point p is located at $r=0$, the following difference formula can be used

$$\frac{\partial u^Y_{ij}}{\partial r} \approx \frac{1}{D}\left[u^Y_{ij}(D,z) - u^Y_{ij}(0,z)\right] \tag{B.3}$$

$$\frac{\partial u^Y_{ij}}{\partial z} \approx \frac{1}{2D}\left[u^Y_{ij}(0,z+D) - u^Y_{ij}(0,z\text{-}D)\right] \tag{B.4}$$

The choice of the interval D is a crucial decision and an extensive numerical investigation is executed in Tonon et al. [51]. The best D value is $10^{-6}R$ where R is the distance between the source and field points.

References

[1] Kermanidis T. A numerical solution for axially symmetrical elasticity problems. *Int J Solids Struct* 1975; 11: 493-500.

[2] Mayr M. On the numerical solution of axisymmetric elasticity problems using an integral equation approach. *Mech Res Com* 1976; 3:393-398.

[3] Cruse TA, Snow DW, Wilson RB. Numerical solutions in axisymmetric elasticity. *Comput Struct* 1977; 7:445-451.

[4] Bakr AA, Fenner RT. Treatment of singular integular integrals in the boundary integral equation method for axisymmetric elastostatics problems. *Communications in Applied Numerical Methods* 1985; 1:81-84.

[5] Becker AA. *The boundary element method in engineering: a complete course*. New York: McGraw-Hill; 1992.

[6] De Lacerda LA, Wrobel LC. Hypersingular boundary integral equation for axisymmetric elasticity. *Int J Num Meth Eng* 2001; 52:1337-1354.

[7] Mukherjee S. Regularization of hypersingular boundary integral equations: a new approach for axisymmetric elasticity. *Eng Anal Bound Elem* 2002; 26: 839-844.

[8] Ishida R, Osaka YQ. On boundary integral equation formulation for axisymmetric problems of transversely isotropic media. *Archive of Applied Mechanics* 1991; 61: 414-421.

[9] Amoura N, Kebir H, Rechak S, Roelandt JM. Axisymmetric and two-dimensional crack identification using boundary elements and coupled quasi-random downhill simplex algorithms. *Eng Anal Bound Elem* 2010; 34(6):611-618.

[10] De Lacerda LA, Wrobel LC. DBEM for axisymmetric crack analysis. *Int J Fract* 2002; 113:267-284.

[11] Watson JO. *Advanced implementation of the boundary element method for two- and three-dimensional elastostatics*. In Developments in Boundary Element Methods-1, Banerjee PK, Butterfield R (eds). Applied Science: London, 1979; 31-63.

[12] Beer G, Watson JO. Infinite boundary elements. *Int J Num Meth Eng* 1989; 28:1233-1247.

[13] Bu S. 3D boundary element analysis of axisymmetric halfspace problems. *Eng Analy Bound Elem* 1996; 17:75-84.

[14] Oliveira MFF, Dumont NA, Selvadurai APS. Boundary element formulation of axisymmetric problems for an elastic halfspace. *Eng Analy Bound Elem* 2012; 36:1478-

1492.

[15] Gibson RE. Some results concerning displacements and stresses in a non-homogeneous elastic half-space. *Geotechnique* 1967; 17: 58-67.

[16] Brown PT, Gibson RE. Surface settlement of a deep elastic stratum whose modulus increases linearly with depth. *Can Geotech J* 1972; 9:467-476.

[17] Awojobi AO. The settlement of a foundation on Gibson soil of the second kind. *Geotechnique* 1975; 25(2): 221-228.

[18] Hirai H. Settlement analysis of rectangular piles in non-homogeneous soil using a Winkler model approach. *Int J Numer Analy Meth Geomech* 2014; 38: 1298-1320.

[19] Rostovtsev NA. On the theory of elasticity of a non-homogeneous medium. *J Appl Math Mech* 1964; 28: 601-611.

[20] Booker JR, Balaam NP, Davis EH. The behavior of an elastic non-homogeneous halfspace: Parts I and II. *Int J Numer Analy Meth Geomech* 1985; 9: 353-367, 369-381.

[21] Rajapakse RKND, Selvadurai APS. Torsion of foundations embedded in non-homogeneous soil in a weathered crust. *Geotechnique* 1989; 39:485-496.

[22] Stark RF, Booker JR. Surface displacements of a non-homogeneous elastic half-space subjected to uniform surface tractions: Parts I and II. *Int J Numer Analy Meth Geomech* 1997; 21:361-378, 379-395.

[23] Yue ZQ, Yin JH, Zhang SY. Computation of point load solutions for geo-materials exhibiting elastic non-homogeneity with depth. *Comput Geotech* 1999; 25:75-105.

[24] Selvadurai APS. The analytical method in geomechanics. *ASME Appl Mech Rev* 2007; 60(3): 87-106.

[25] Selvadurai APS, Katebi A. Mindlin's problem for an incompressible elastic half-space with an exponential variation in the linear elastic shear modulus. *Int J Eng Sci* 2013; 65:9-21.

[26] Katebi A, Selvadurai APS. Undrained behavior of a non-homogeneous elastic medium: the influence of variations in the elastic shear modulus with depth. *Geotechnique* 2013; 63:1159-1169.

[27] Jaeger JC, Cook NGW, Zimmerman RW. *Fundamentals of rock mechanics*, 4th Edn. Blackwell Publishing, 2007.

[28] Chen WT. Computation of the stresses and displacements in a layered elastic medium. *Int*

J Eng Sci 1971; 9:775-800.

[29] Yue ZQ, Wang R. Static solutions for transversely isotropic elastic N-layered systems. *Acta Scientiarum Naturalium Universitatis Pekinensis* 1998; 24:202-211.

[30] Pan E. Static response of a transversely isotropic and layered halfspace to general surface loads. *Phys Earth Planet Inter* 1989; 54:353-363.

[31] Alkasawneh W, Pan E, Han F, Zhu R, Green R. Effect of temperature variation on pavement responses using 3D multilayered elastic analysis. *Int J Pavement Engineering* 2007; 8(3): 203-212.

[32] Pan E, Bevis M, Han F, Zhou H, Zhu R. Surface deformation due to loading of a layered elastic half-space: a rapid numerical kernel based on a circular loading element. *Geophys J Int* 2007; 171:11-24.

[33] Xiao HT, Yue ZQ, Zhao XM. A generalized Kelvin solution based method for analyzing elastic fields in heterogeneous rocks due to reservoir water impoundment. *Comput Geosci* 2012; 43:126-136.

[34] Yue ZQ. On cause hypotheses of earthquakes with external tectonic plate and/or internal dense gas loadings. *Acta Mech* 2014; 225:1447-1469.

[35] Bakr AA. *The boundary integral equation method in axisymmetric stress analysis problems*. Berlin: Springer-Verlag; 1985.

[36] Pan E. Green's functions for geophysics: a review. *Rep Prog Phys* 2019; 82,106801.

[37] Xiao S, Yue ZQ, Xiao HT. Boundary element analysis of elastic fields in non-horizontally layered halfspace whose horizontal boundary subject to tractions. *Eng Anal Bound Elem* 2018; 95:105-123.

[38] Xiao S, Yue ZQ, Xiao HT. Boundary element analysis of transversely isotropic bi-material halfspaces with inclined planes of isotropy and interfaces. *Int J Numer Analy Meth Geomech* 2019; 43:2599-2627.

[39] Xiao S, Yue ZQ, Xiao HT. Dual boundary element method for analyzing three-dimensional cracks in horizontally layered halfspaces. *Eng Anal Bound Elem* 2019; 104:135-147.

[40] Yue ZQ. On generalized Kelvin solutions in a multilayered elastic medium. *J Elast* 1995; 40:1-43.

[41] Yue ZQ. Yue's solution of classical elasticity in *n*-layered solids: Part 1, mathematical

formulation. *Front Struct Civ Eng* 2015; 9:215-249.

[42] Yue ZQ. Yue's solution of classical elasticity in *n*-layered solids: Part 2, mathematical verification. *Front Struct Civ Eng* 2015; 9:250-285.

[43] Maloney JM, Walton EB, Bruce CM, Van Vliet KJ. Influence of finite thickness and stiffness on cellular adhesion-induced deformation of compliant substrata. *Physical Review E* 2008; 78:041923.

[44] Buxboim A, Rajagopal K, Brown AEX, Discher DE. How deeply cells feel: methods for thin gels. *J Phys*: *Condens Matter* 2010; 22:194116.

[45] Merkel R, Kirchgeßner N, Cesa CM, Hoffmann B. Cell force microscopy on elastic layers of finite thickness. *Biophysical Journal* 2007; 93(9):3314-3332.

[46] Almeida Pereira OJB, Parreira P. Direct evaluation of Cauchy-principal-value integrals in boundary elements for infinite and semi-infinite three-dimensional domains. *Eng Anal Bound Elem* 1994; 13:313-320.

[47] Moser W, Duenser Ch, Beer G. Mapped infinite elements for 3D multi-region boundary element analysis. *Int J Numer Meth Eng* 2004; 61:317-328.

[48] Xiao HT, Yue ZQ. *Fracture mechanics in layered and graded materials: analysis using boundary element methods*. Berlin: De Gruyter and Beijing: Higher Education Press; 2014.

[49] Timoshenko SP, Goodier JN. *Theory of elasticity,* 3rd Edn. The McGraw-Hill Company; 1970.

[50] Kutt HR. *Quadrature formulae for finite-part integrals*. Special Report WISK 178, National Research Institute for Mathematical Sciences, Pretoria, 1975.

[51] Tonon F, Pan E, Amadei B. Green's functions and boundary element method formulation for 3D anisotropic media. *Comput Struct* 2001; 79:469-482.

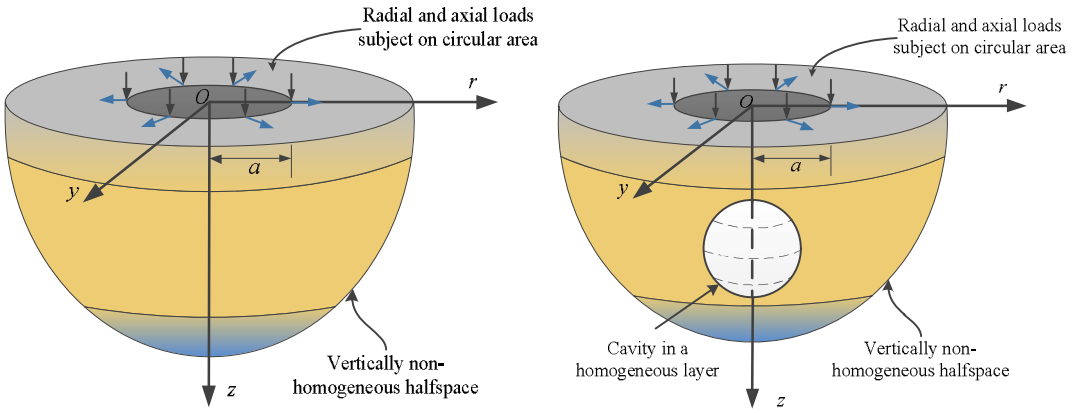

(a) (b)

Fig. 1. Typical axisymmetric problems in vertically non-homogeneous solids subject to traction: (a) without and (b) with a cavity

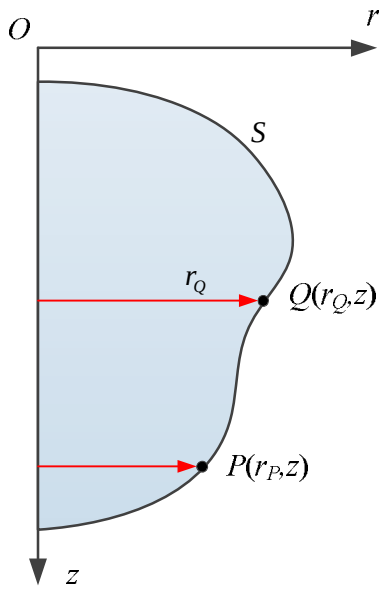

Fig. 2. Definition of the integral domain for BEM analysis of axisymmetric problems in a homogeneous solid

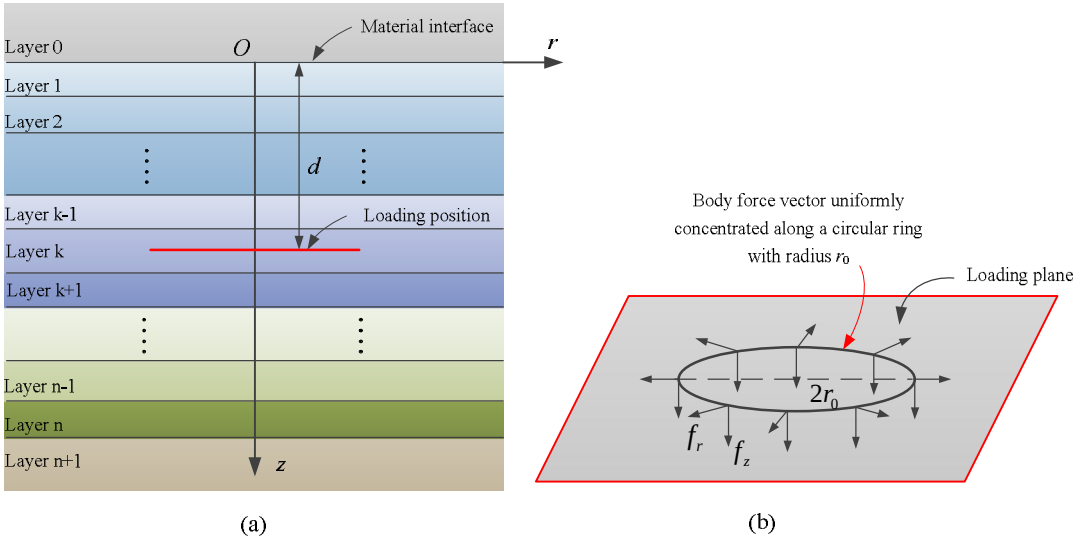

Fig. 3. A multilayered elastic solid of infinite extent subject to a body force vector uniformly concentrated along a circular ring horizontally placed at depth *d*

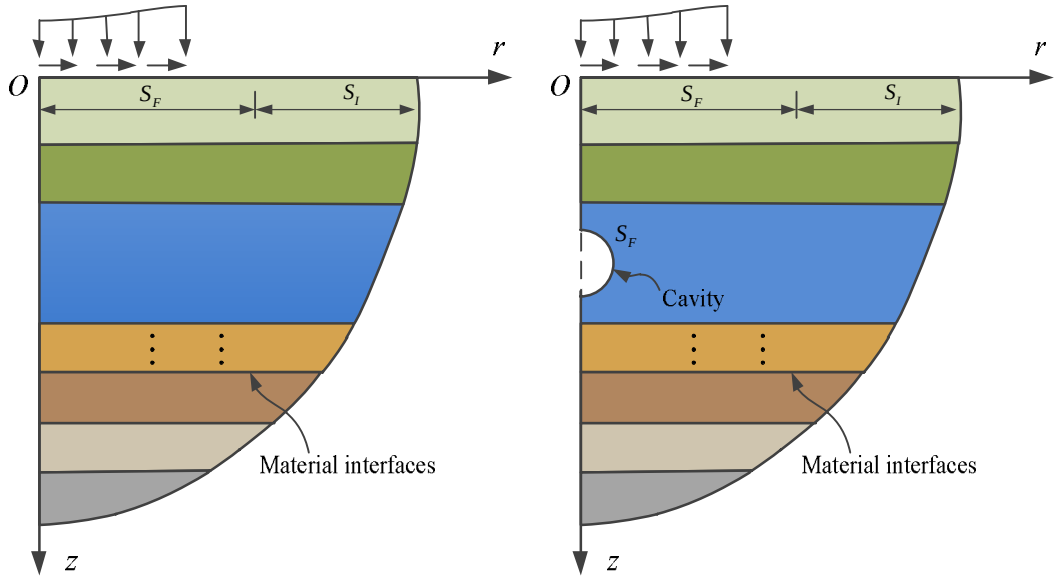

Fig. 4. BEM analysis of axisymmetric problems in a layered solid subject to traction: (a) without cavity and (b) with a cavity

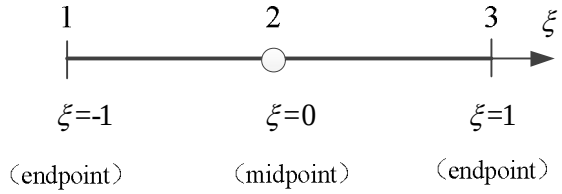

(a) A finite boundary element with three node points at 1, 2, and 3

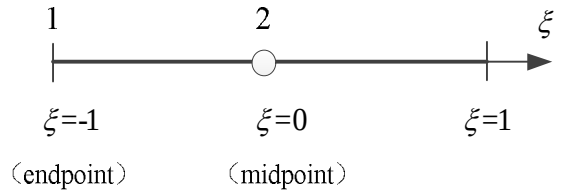

(b) An infinite boundary element with two node points at 1 and 2

Fig. 5. The two types of line (1-D) boundary elements for BEM analysis of axisymmetric problems: (a) finite region and (b) semi-infinite region

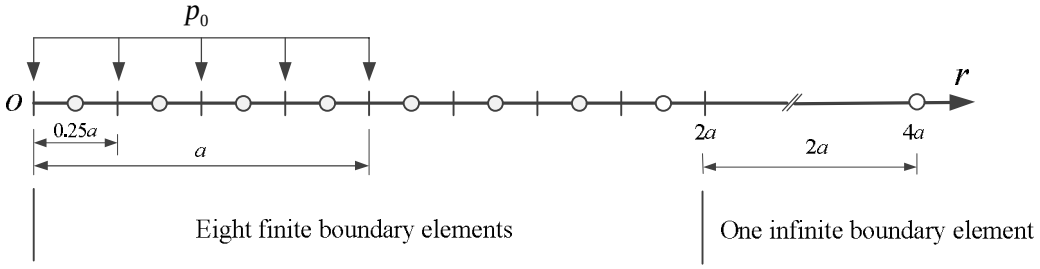

Fig. 6. Discretization mesh of the axisymmetric boundary surface of a halfspace into eight finite boundary elements and one infinite boundary element

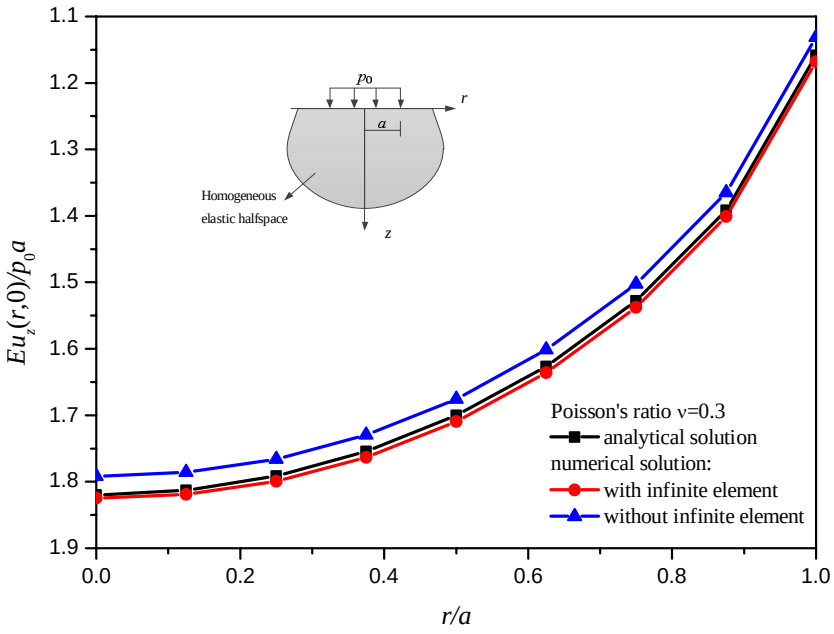

Fig. 7. Comparison of three results for the vertical displacement at the boundary surface of a homogeneous elastic halfspace subject to uniform normal traction over a circular area

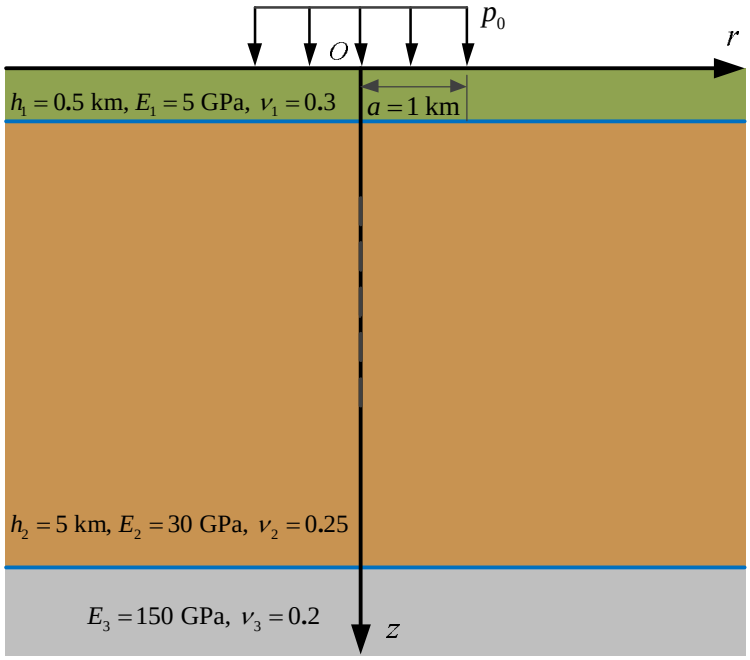

Fig. 8. Axisymmetric problem of a two-layered elastic halfspace whose boundary surface subject to uniform normal traction over a circular area

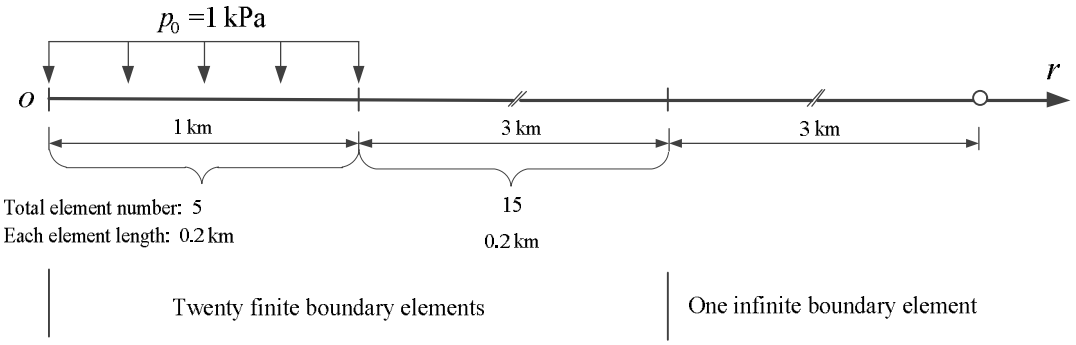

Fig. 9. Discretization mesh of the axisymmetric boundary surface of a halfspace into twenty finite elements and one infinite element

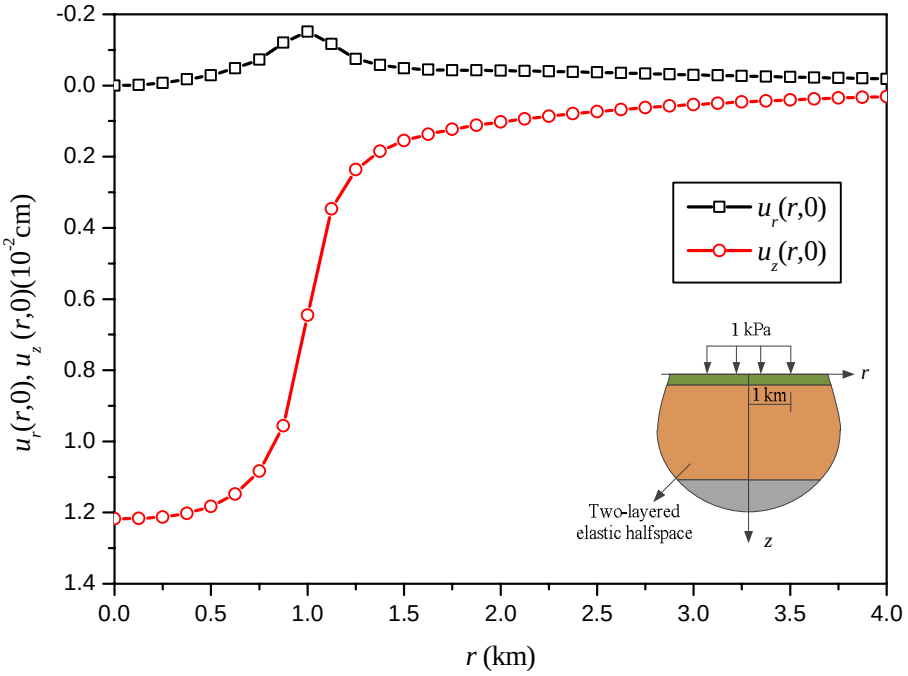

Fig. 10. BEM results of the radial and vertical displacements (u_r and u_z) on the boundary surface of the two-layered halfspace due to the uniform normal traction over a circular area

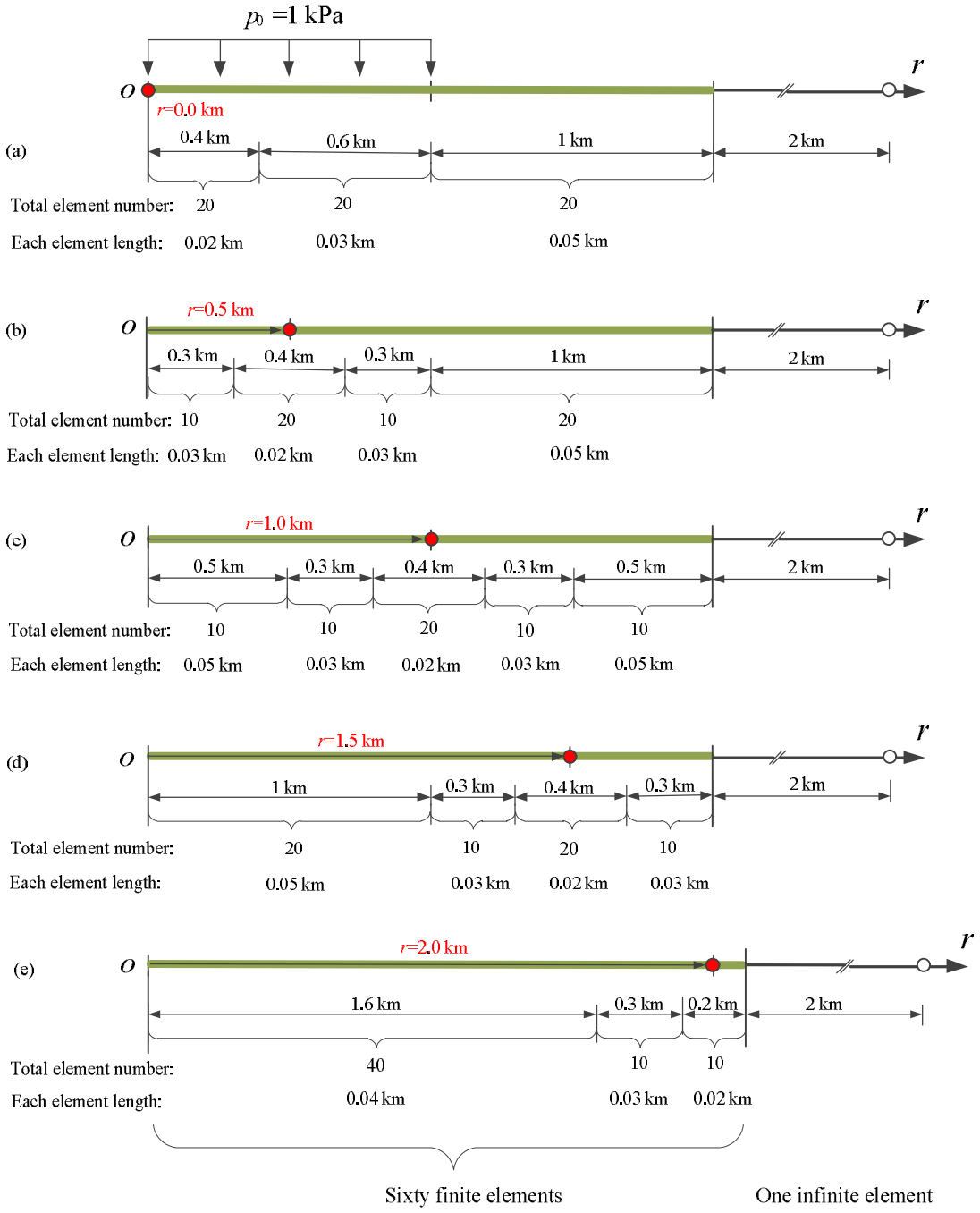

Fig. 11. Five different discretization meshes of the axisymmetric boundary surface of a halfspace into sixty finite elements and one infinite element: (a) r = 0.0 km, (b) r = 0.5 km, (c) r = 1.0 km, (d) r = 1.5 km, and (e) r = 2.0 km

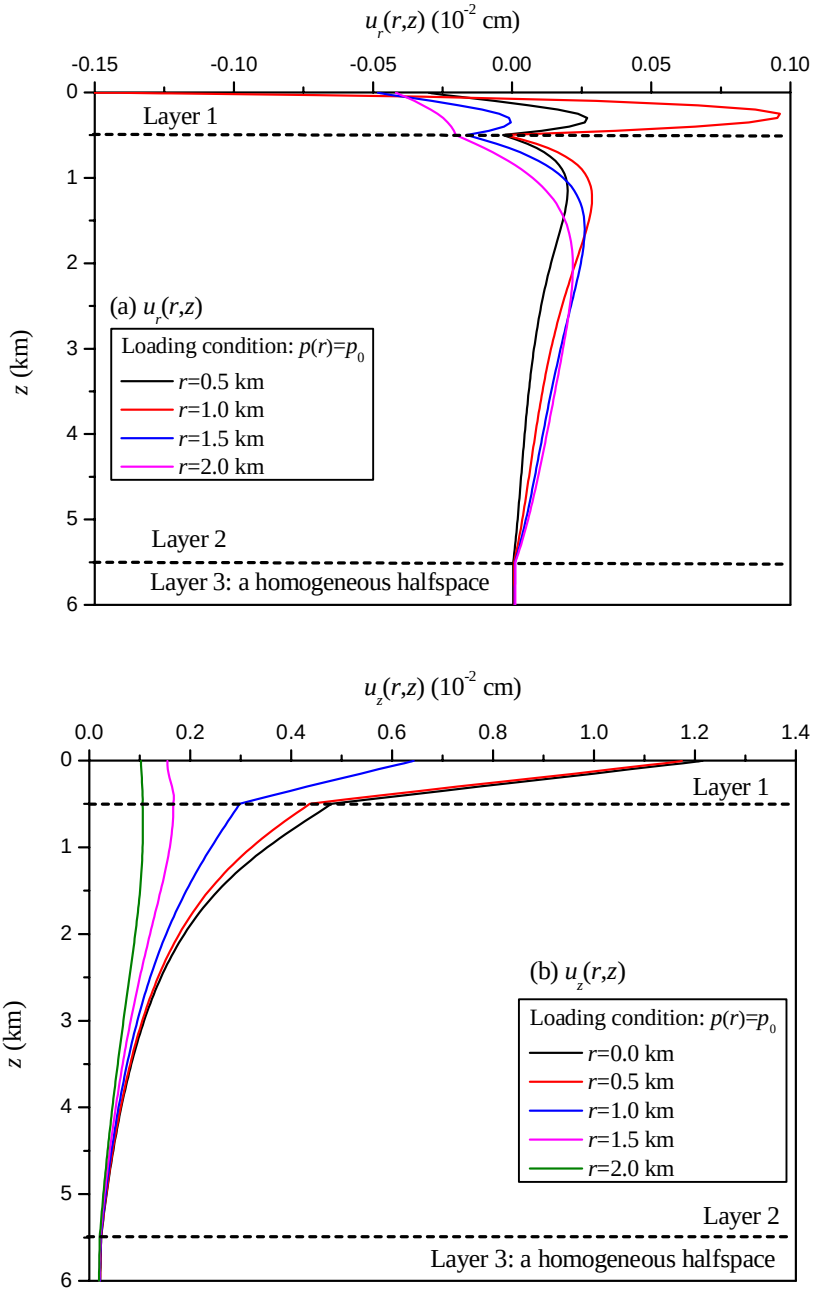

Fig. 12. Variations of displacements with the depth in the two-layered halfspace subject to a uniform normal traction over a circular area: (a) the horizontal displacement u_r at four radial distance locations and (b) the vertical displacement at five radial distance locations

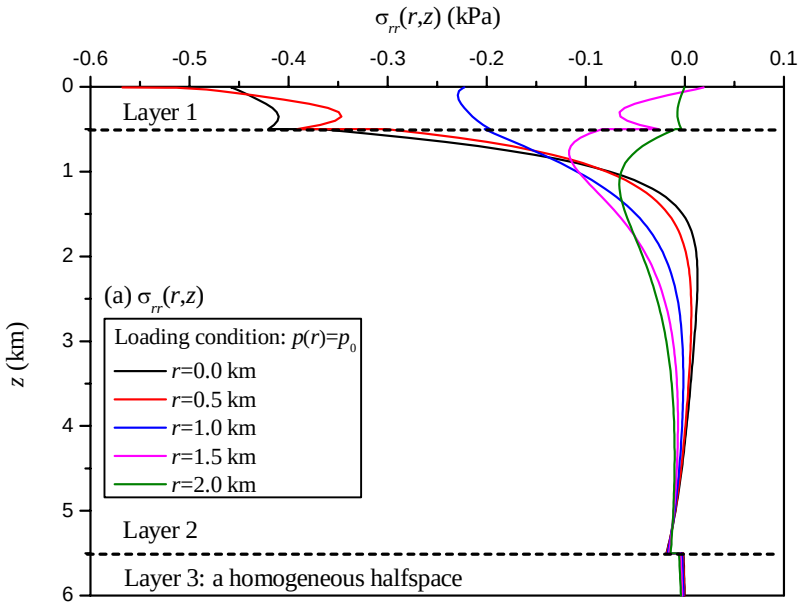
σrr(r,z) (kPa)
-0.6
-0.5
-0.4
-0.3
-0.2
-0.1
0.0
0.1
0
1
2
3
4
5
6
z (km)
Layer 1
(a) σrr(r,z)
Loading condition: p(r)=p0
r=0.0 km
r=0.5 km
r=1.0 km
r=1.5 km
r=2.0 km
Layer 2
Layer 3: a homogeneous halfspace

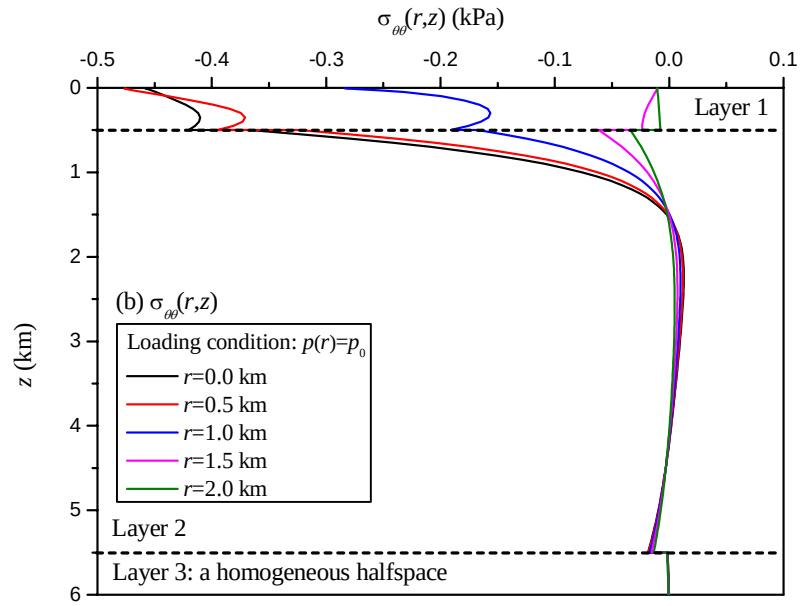
σθθ(r,z) (kPa)
-0.5
-0.4
-0.3
-0.2
-0.1
0.0
0.1
0
1
2
3
4
5
6
z (km)
Layer 1
(b) σθθ(r,z)
Loading condition: p(r)=p0
r=0.0 km
r=0.5 km
r=1.0 km
r=1.5 km
r=2.0 km
Layer 2
Layer 3: a homogeneous halfspace

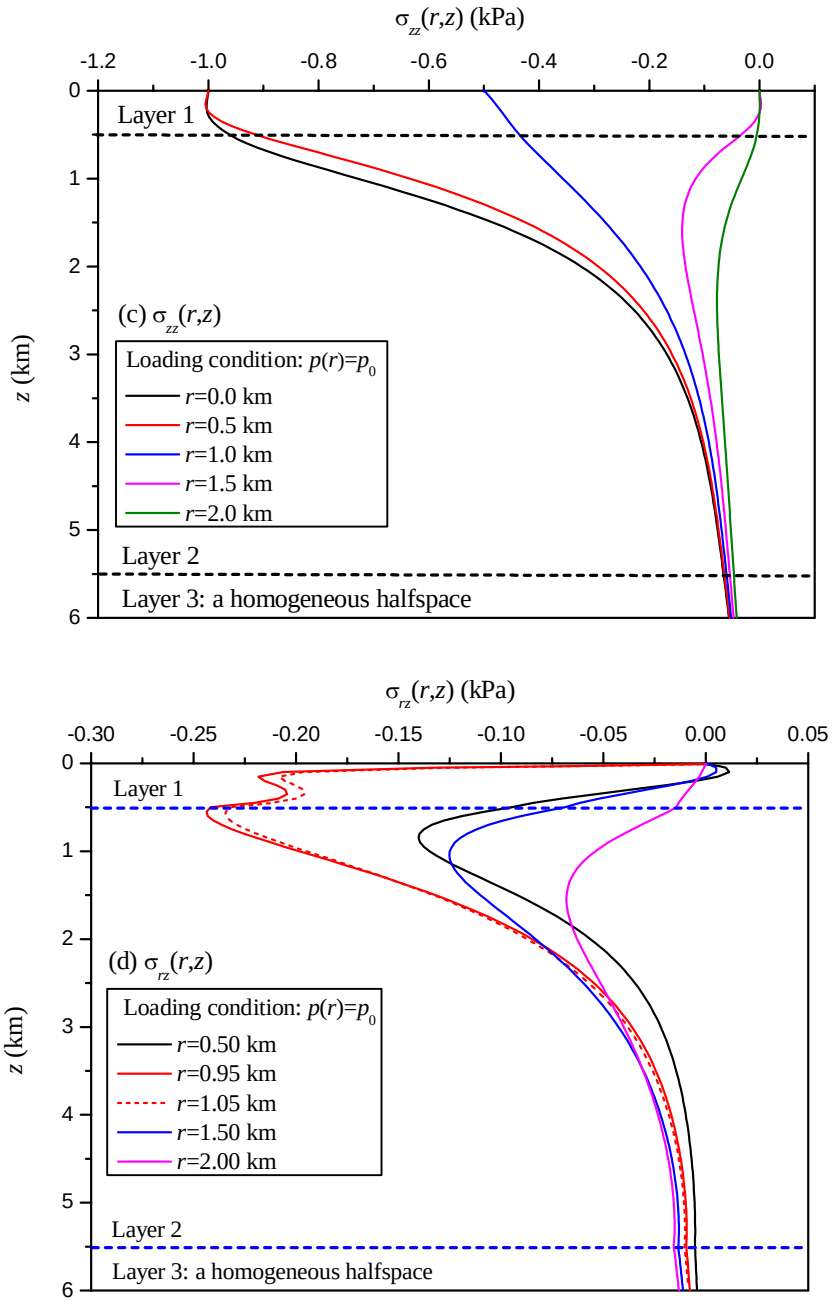

Fig. 13. Variations of the four stress components with depth at five radial distances in the two-layered halfspace subject to a uniform normal traction over a circular area: (a) σ_{rr}, (b) $\sigma_{\theta\theta}$, (c) σ_{zz}, and (d) σ_{rz}

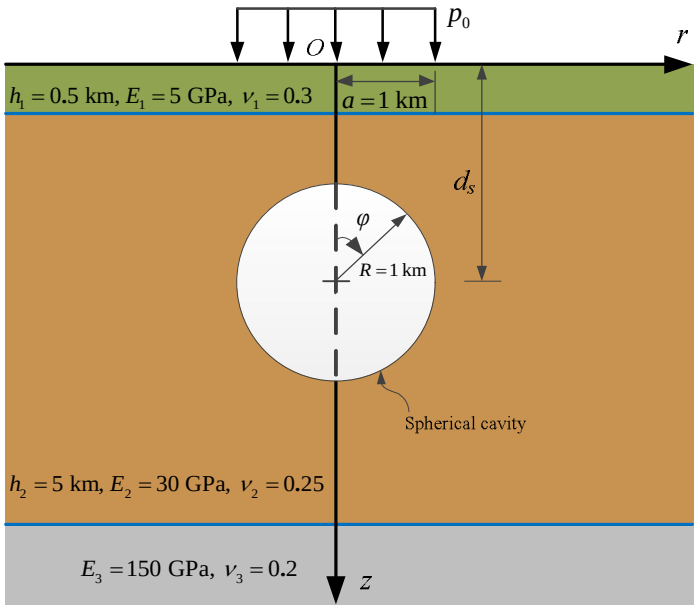

Fig. 14. Axisymmetric problem of a two-layered elastic halfspace with a spherical cavity at depth d_s subject to uniform normal traction over a circular area

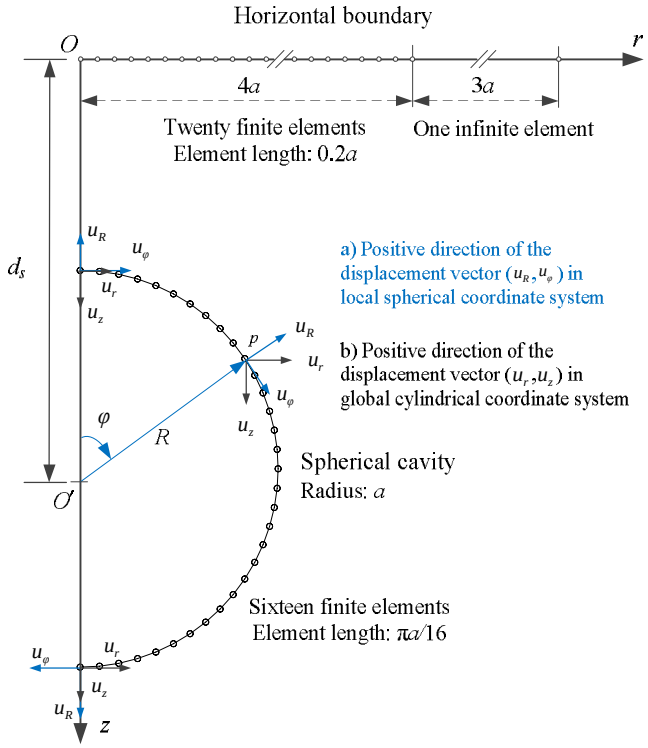

Fig. 15. BEM discretization mesh of the horizontal external boundary and the internal cavity boundary of the layered halfspace with a spherical cavity

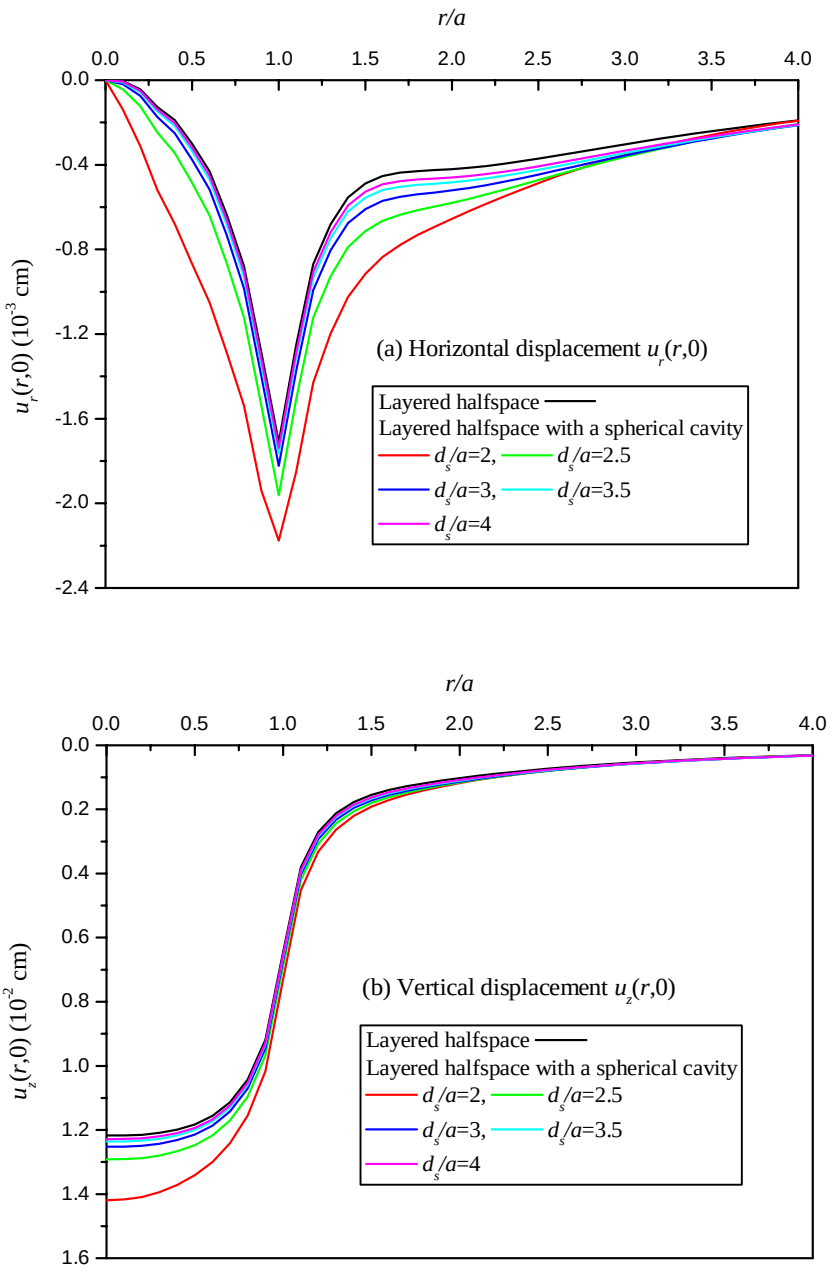

Fig. 16. Variations of the displacements with radial distance on the horizontal external boundary of the two-layered halfspace without and with a spherical cavity subject to a uniform normal traction over a circular area: (a) the horizontal radial displacement u_r, (b) the vertical displacement u_z

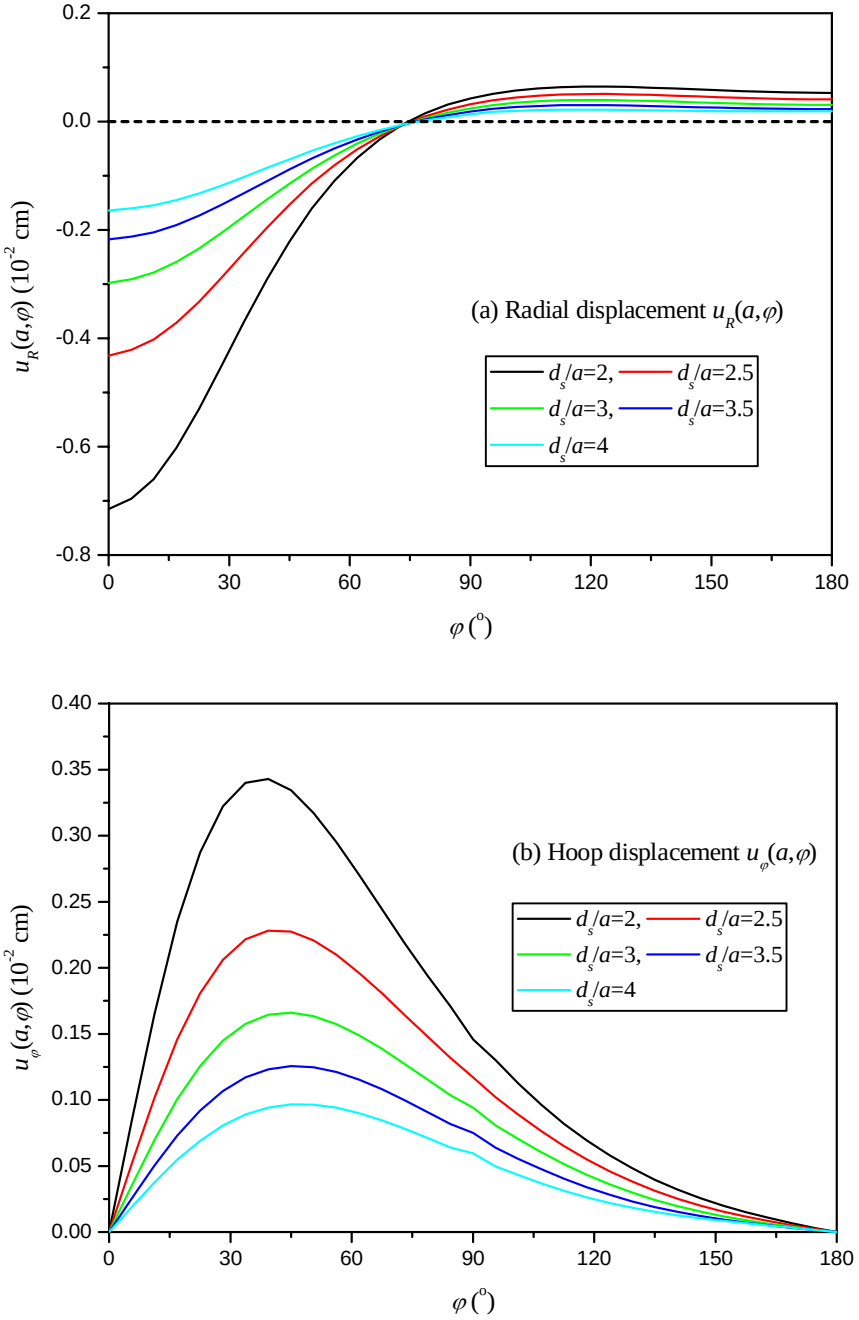

Fig. 17. Variations of the displacements with the hoop angle φ on the internal boundary surface of a spherical cavity in the two-layered halfspace whose external boundary surface subject to a uniform normal traction over a circular area: (a) the radial displacements u_R, (b) the hoop displacement u_φ

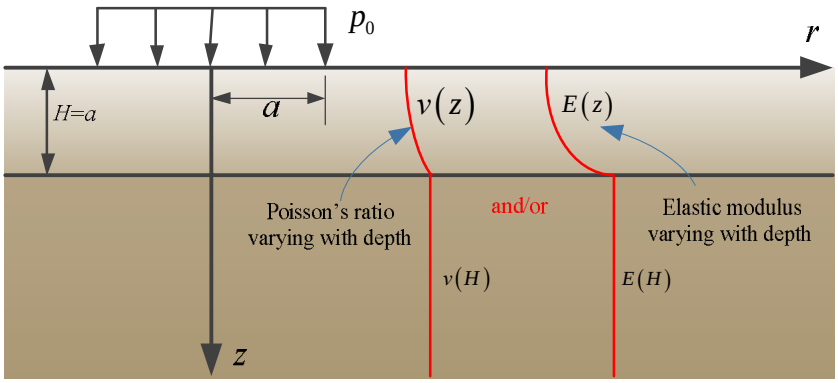

Fig. 18. An axisymmetric problem of a vertically non-homogeneous solid with modulus and Poisson's ratio arbitrarily variable with depth subject to a uniform normal traction over a circular area

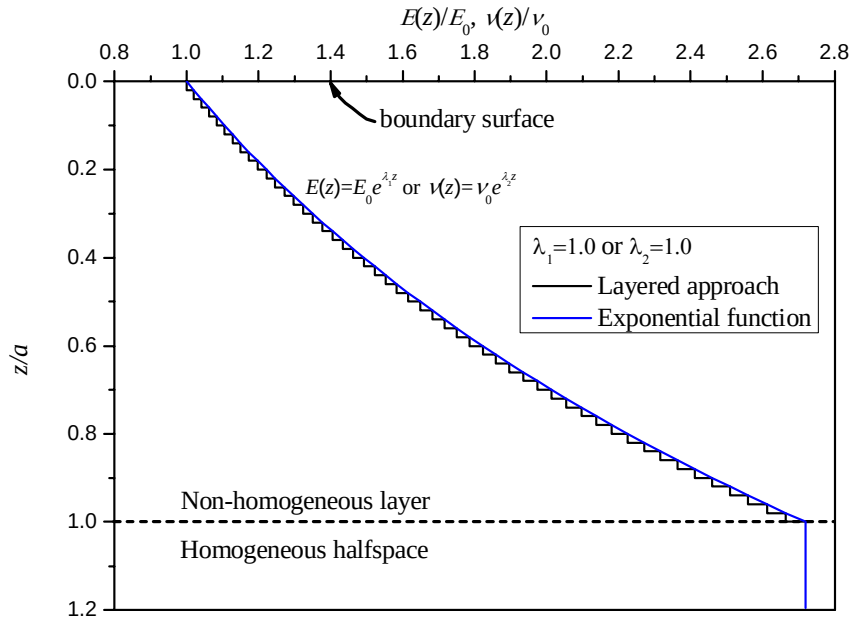

Fig. 19. Approximation of the continuous depth variation of the elastic modulus and Poisson's ratio by a layered system of 50 dissimilar homogeneous thin layers

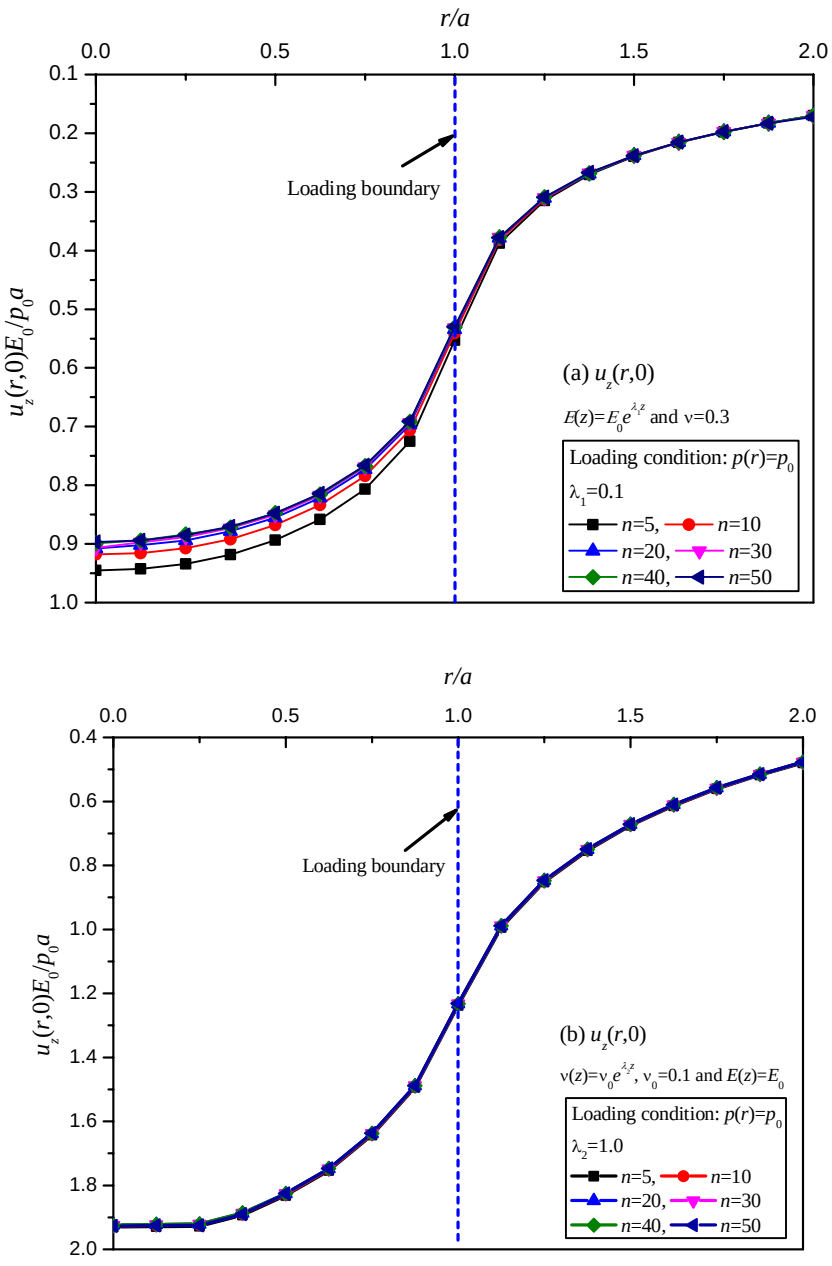

Fig. 20. Comparisons of the six vertical displacement results from six *n* values of the thin layer number for the vertical non-homogeneous solid subject to a uniform normal traction: (a) approximation of elastic modulus and (b) approximation of the Poisson's ratio

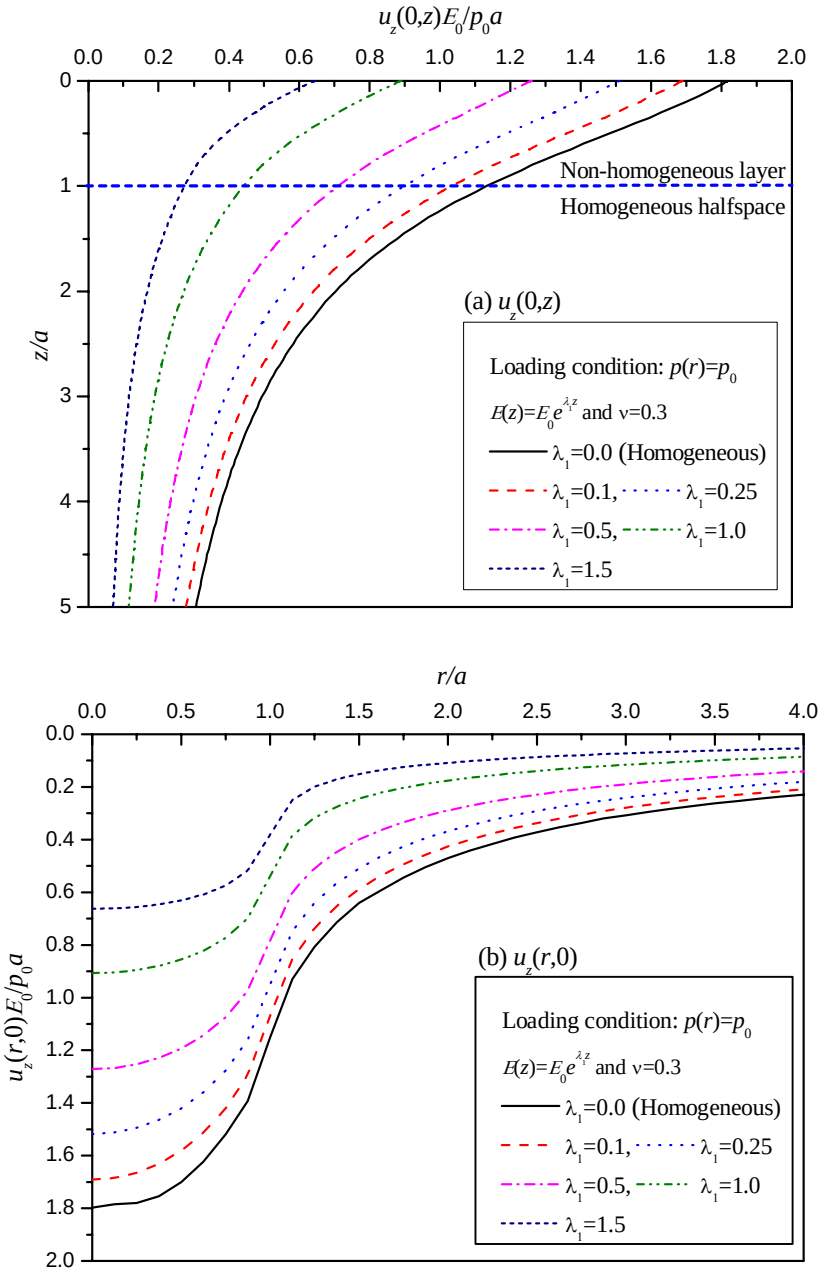

Fig. 21. Variations of the vertical displacement results for six λ_1 values of a vertically non-homogeneous solid subject to a uniform normal traction over a circular area: (a) vertical displacement at the center with depth, (b) the vertical displacement at boundary surface with the horizontal radial distance

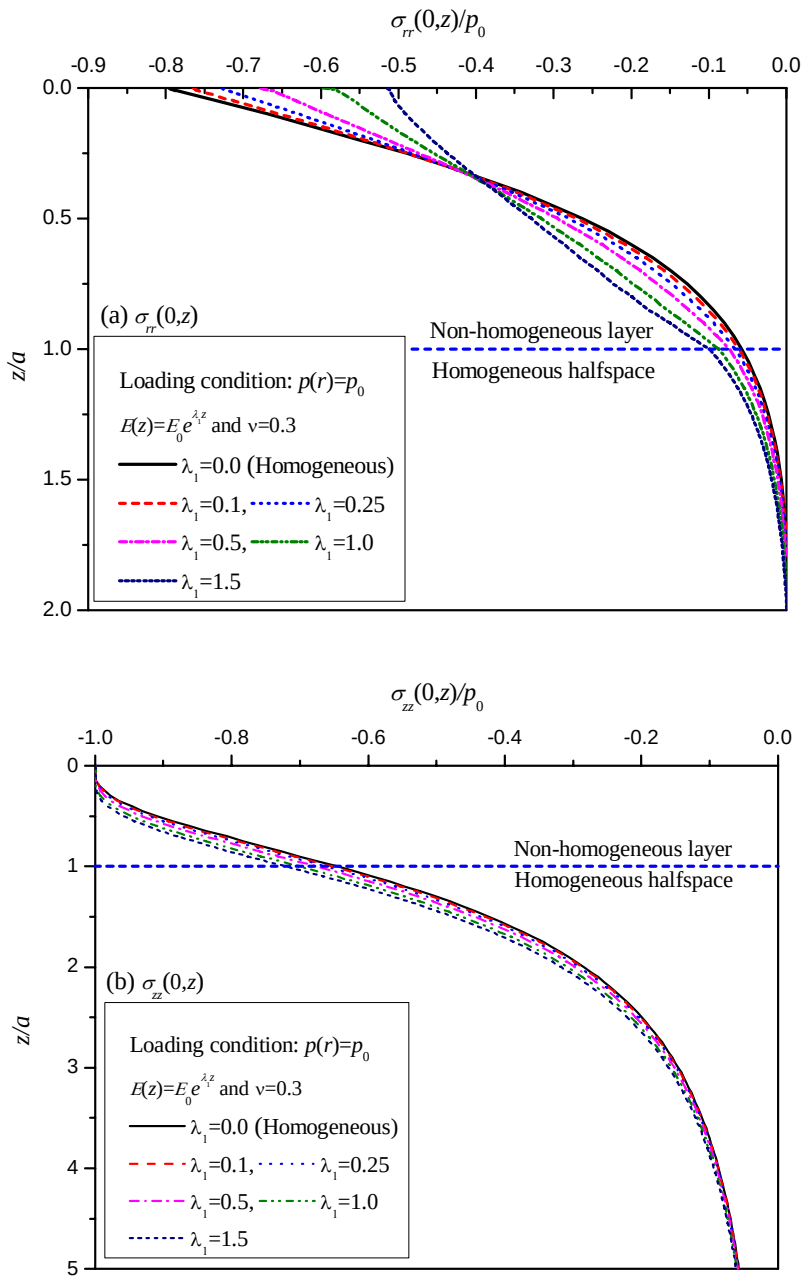

Fig. 22. Variations of the two normal stresses at the center with depth for six λ_1 values of a vertically non-homogeneous solid subject to a uniform normal traction over a circular area: (a) the radial normal stress $\sigma_{rr}(0,z)/p_0$, (b) the vertical normal stress $\sigma_{zz}(0,z)/p_0$

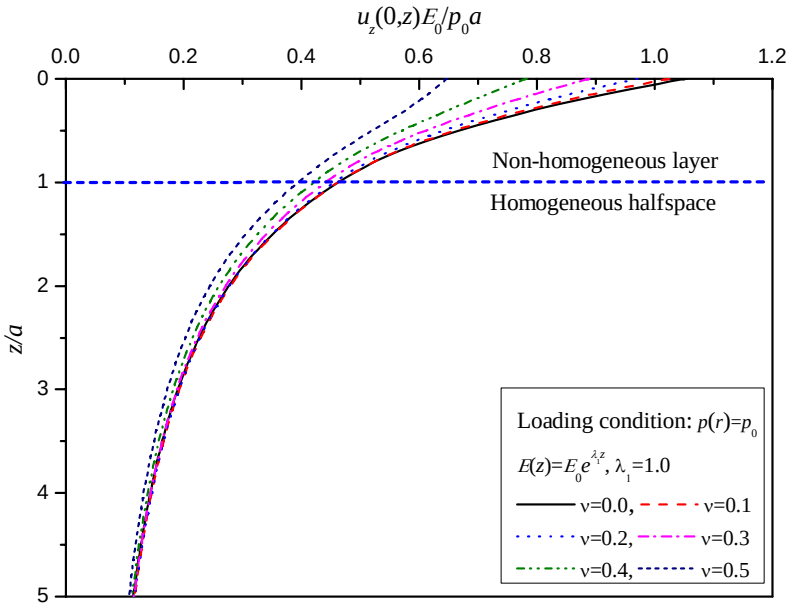

Fig. 23. Depth variations of the vertical displacement results for six Poisson's ratio values of a vertically non-homogeneous solid subject to a uniform normal traction over a circular area

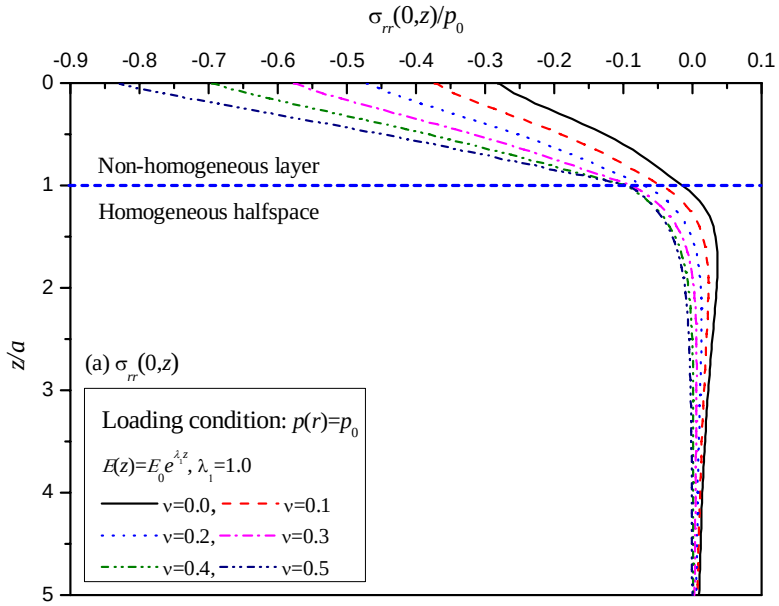

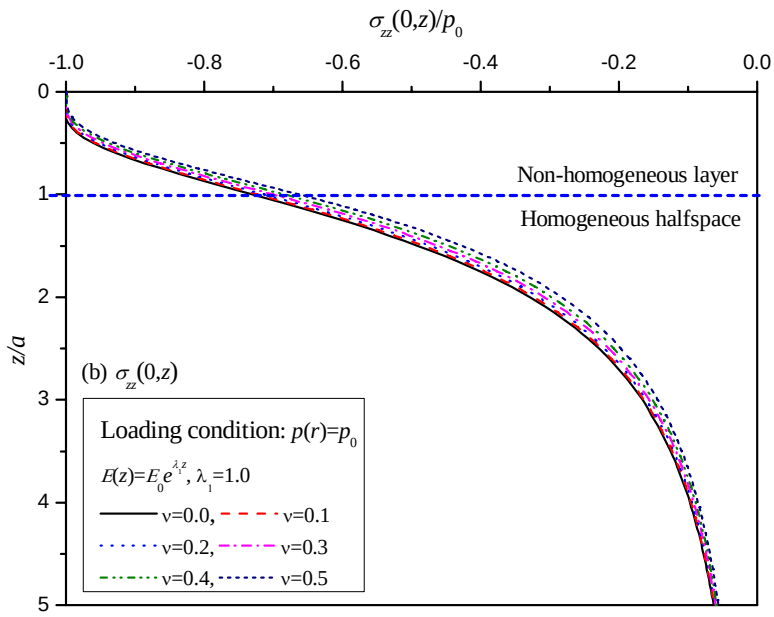

Fig. 24. Depth variations of the two normal stress results for six Poisson's ratio values of a vertically non-homogeneous solid subject to a uniform normal traction over a circular area: (a) the radial normal stress $\sigma_{rr}(0,z)/p_0$, (b) the vertical normal stress $\sigma_{zz}(0,z)/p_0$

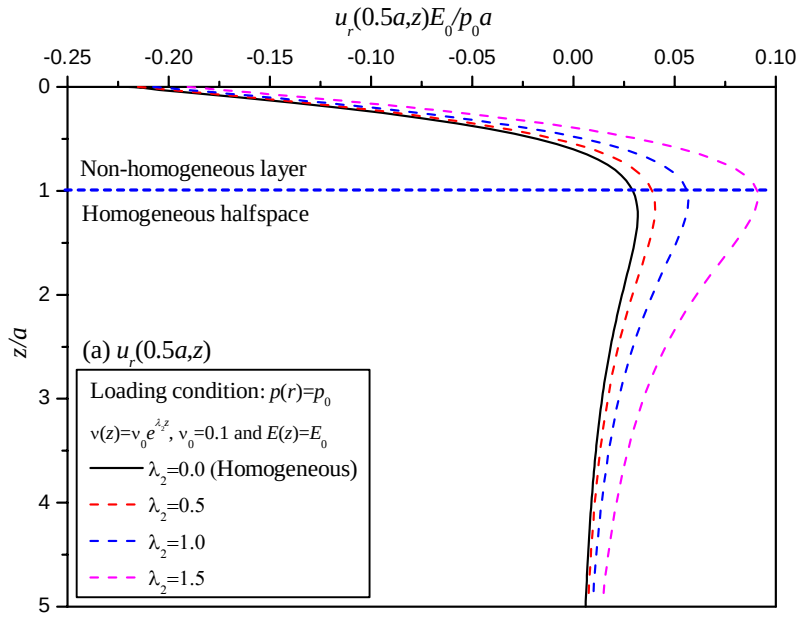

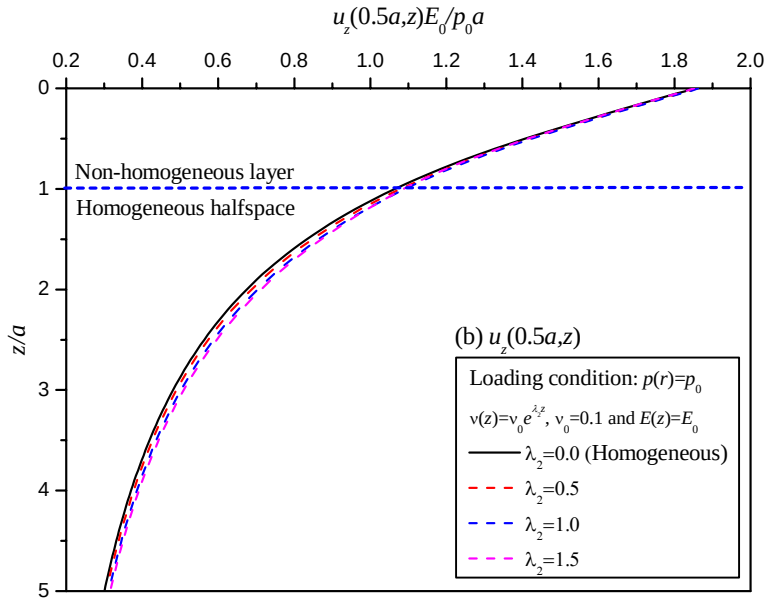

Fig. 25. Depth variations of the two displacements for four λ_2 values of a vertically non-homogeneous solid subject to a uniform normal traction over a circular area: (a) the horizontal radial displacement $E_0 u_r(0.5a,z)/p_0a$, (b) the vertical displacement $E_0 u_z(0.5a,z)/p_0a$

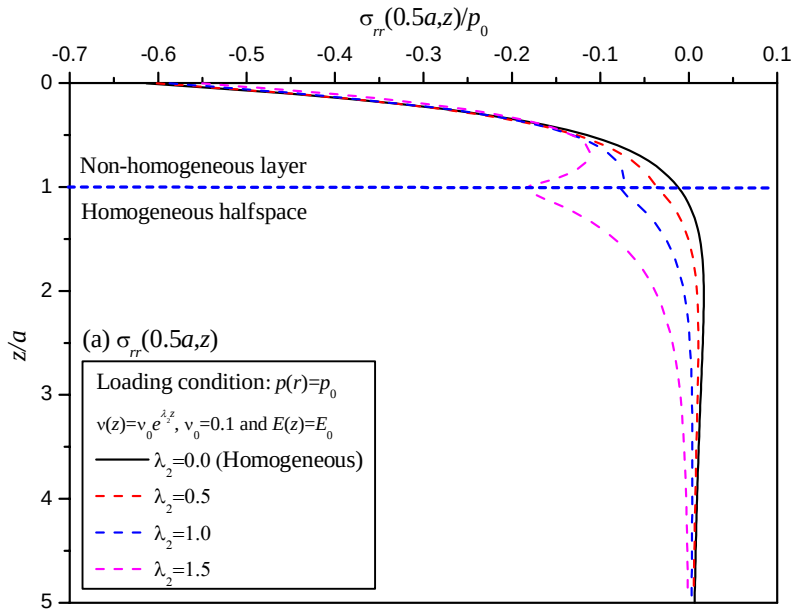

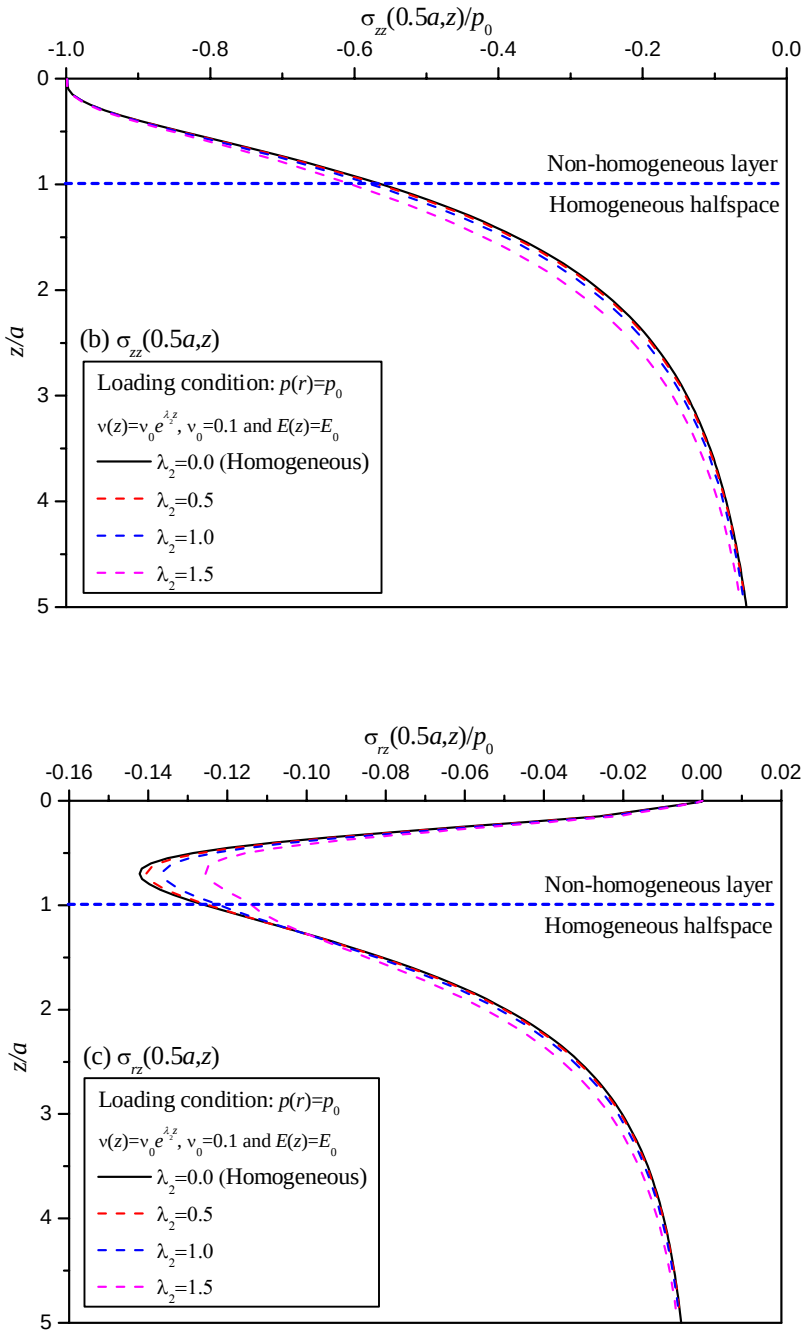

Fig. 26. Depth variations of the three stresses for four λ_2 values of a vertically non-homogeneous solid subject to a uniform normal traction over a circular area: (a) the radial normal stress $\sigma_{rr}(0.5a,z)/p_0$, (b) the vertical normal stress $\sigma_{zz}(0.5a,z)/p_0$, and (c) the radial shear stress $\sigma_{rz}(0.5a,z)/p_0$

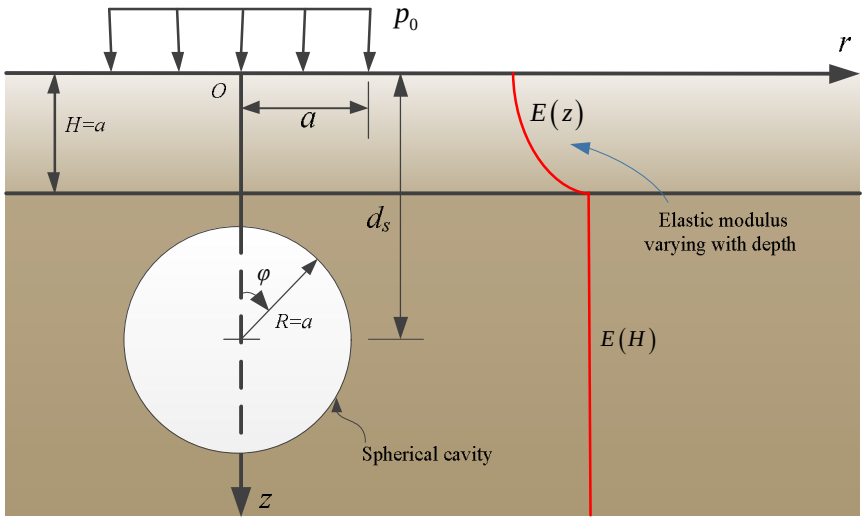

Fig. 27. Axisymmetric problem of a vertically non-homogeneous halfspace with a spherical cavity whose external boundary surface subject to uniform normal traction over a circular area

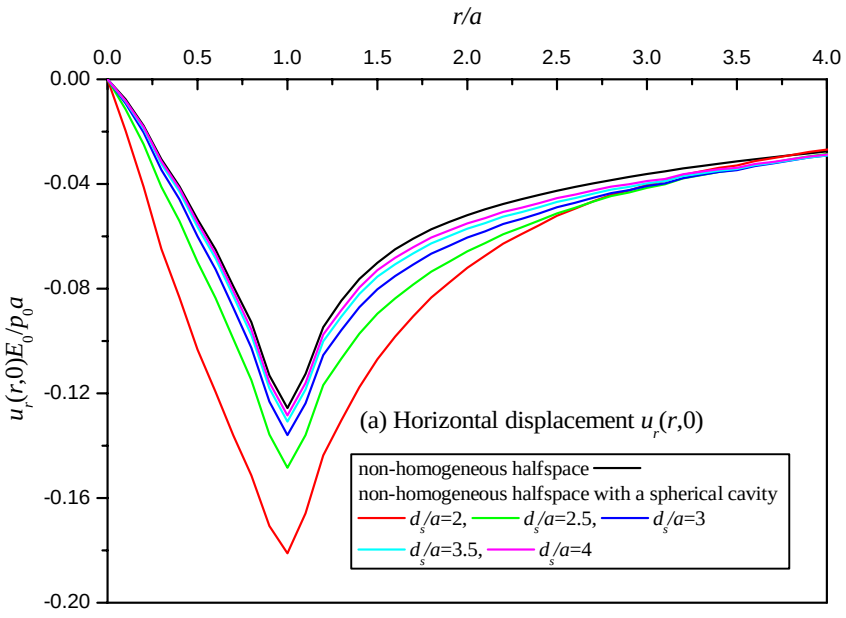

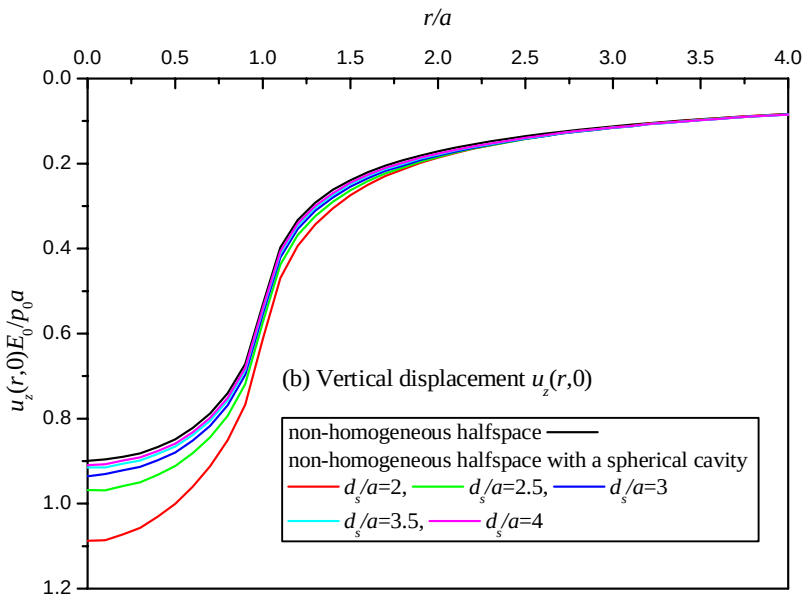

Fig. 28. Variations of the two displacements with the radial distance on the external horizontal boundary of a vertically non-homogeneous solid without and with a spherical cavity subject to a uniform normal traction over a circular area: (a) the horizontal radial displacement u_r, (b) the vertical displacement u_z

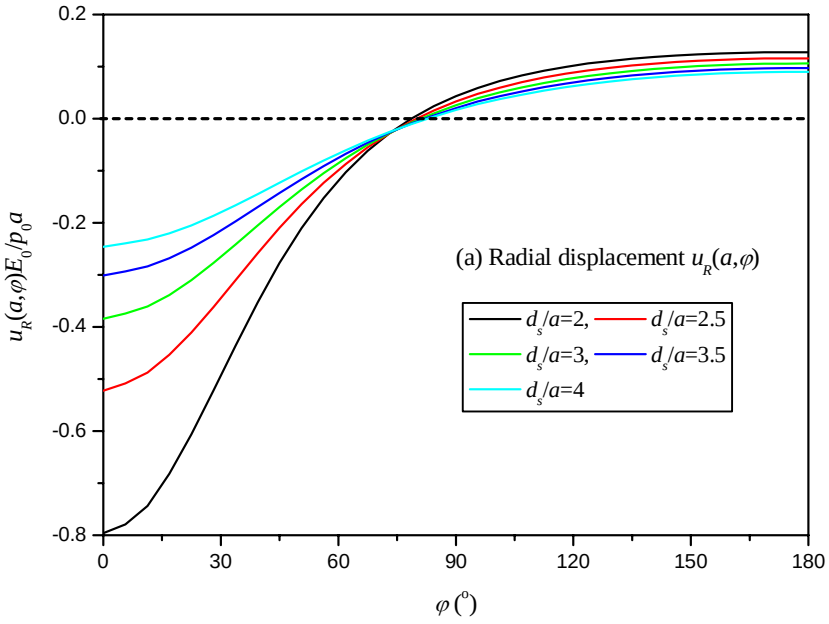

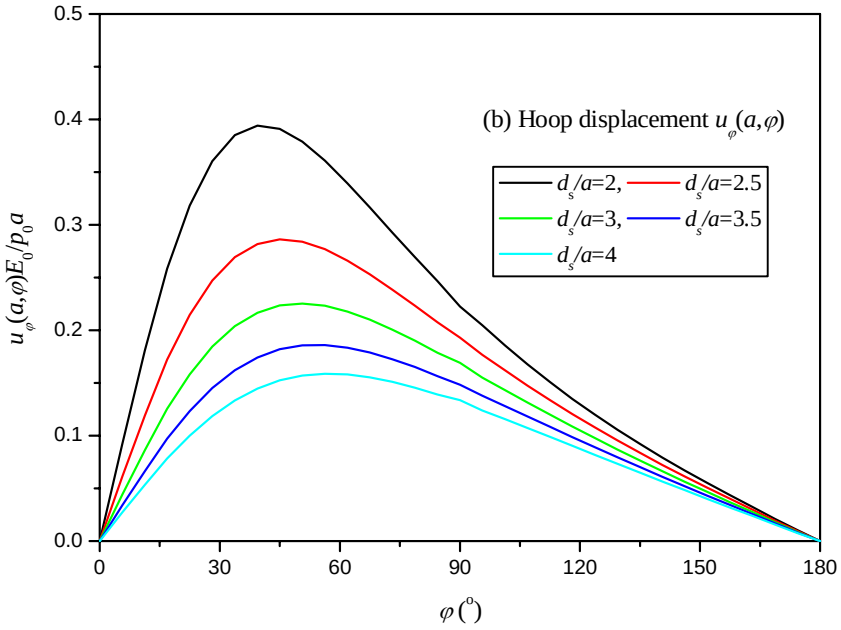

Fig. 29. Variations of the displacements with the hoop angle φ on the internal boundary surface of a spherical cavity in the vertically non-homogeneous halfspace whose external boundary surface subject to a uniform normal traction over a circular area: (a) the radial displacements u_R, (b) the hoop displacement u_φ

Table. 1 Comparison of the radial and vertical normal stresses at the material interface and their relative errors

$(r/a, z/a)$	σ_{rr} / p_0			σ_{zz} / p_0		
	Present	Chen [28]	Relative error	Present	Chen [28]	Relative error
$(1.0,0.8\text{-}10^{-5})$	-0.11009	-0.10881786	1.17%	-0.23852	-0.23769637	0.035%
$(1.0,0.8\text{+}10^{-5})$	-0.11795	-0.11576585	1.88%	-0.23856	-0.23769637	0.036%

Table. 2 Organization of BEM examples in this paper

Sections	BEM examples	Purposes	Calculation information
5.4	Layered halfspace	Investigate the depth variations of displacements and stresses	$E_1 = 5\text{GPa}$, $E_2 = 30\text{GPa}$, $E_3 = 150\text{GPa}$, $v_1 = 0.3$, $v_2 = 0.25$, $v_3 = 0.2$, $h_1 = 0.5\text{km}$, $h_2 = 5\text{km}$
	Spherical cavity in a layered halfspace	Investigate the variations of displacements on the boundaries	
6.2	Vertically non-homogeneous halfspaces	Investigate the variations of displacements and stresses for different λ_1 of non-homogeneous halfspaces with elastic modulus varying with depth	λ_1= 0.1, 0.25, 0.5, 1, 1.5 λ_2= 0, ν_0=0.3
		Investigate the variations of displacements and stresses for different Poisson's ratios of non-homogeneous halfspaces with elastic modulus varying with depth	λ_1= 1 $\nu(z)$=0, 0.1, 0.2, 0.3, 0.4, 0.5
		Investigate the variations of displacements and stresses for different λ_2 of non-homogeneous halfspaces with Poisson's ratio varying with depth	$E(z)=E_0$, ν_0=0.1, λ_2= 0.5, 1, 1.5
6.3	Spherical cavity in a vertically non-homogeneous halfspace	Investigate the variations of displacements on the boundaries	λ_1=1, $\nu(z)$=0.3; d_s/a = 2.0, 2.5, 3.0, 3.5, 4.0

Table. 3 Summary of key findings and conclusions

Aspects	Key findings
Boundary element techniques	(1) In this BEM, Yue's solution is used to eliminate the requirement of mesh discretization for the internal material interface planes and only the horizontal boundary surface of a halfspace and the boundary of a cavity need to be discretized. (2) The core region around the traction area can be discretized using finite isoparametric elements and the far-field region beyond the traction area can be discretized using one infinite boundary element. (3) The infinite boundary element is used to effectively and efficiently take into account the influence of a far region to a core region around the loading area.
Numerical results and verifications	(4) The numerical verifications illustrate that this BEM can obtain the accurate results of axisymmetric problems in vertically non-homogeneous solids. (5) The two displacements (u_r and u_z) and the vertical stresses (σ_{zz} and σ_{rz}) are non-smoothly continuous across the material interfaces whereas the plane stresses (σ_{rr} and $\sigma_{\theta\theta}$) are discontinuous at the material interfaces. (6) When the elastic modulus varies with depth, the elastic modulus has an evident effect on displacements. (7) When the Poisson's ratio varies with depth, the Poisson's ratio has a significant influence on the displacement u_r and the stress components (σ_{rr} and σ_{rz}). (8) The position of the spherical cavity significantly affects the displacements on the boundaries of the layered and non-homogeneous halfspaces.